Chapter 6

Energy Efficiency of Electric Vehicles – Energy Saving and Optimal Control Technologies

Guoqing Xu, Chunhua Zheng, Yanhui Zhang,
Kun Xu and Jianing Liang

Additional information is available at the end of the chapter

http://dx.doi.org/10.5772/59420

1. Introduction

Electric vehicles (EVs), including pure electric vehicles (PEVs or EVs), hybrid electric vehicles (HEVs), and fuel cell vehicles (FCVs), have attracted worldwide attention increasingly from governments, industry, and public. Though EVs have shown advantages over internal combustion engine (ICE) vehicles in terms of environmental friendliness and energy efficiency, there are still many technical challenges impeding the market share growth.

In this chapter, the energy-related issues for EVs will be discussed in detail. The primary aim of this chapter is to give a clear and systematic understanding of the energy processing and control for EVs and to introduce some latest energy saving and optimal control technologies and present the key results regarding this area. The overall technical architecture and the overview of the state of the art will be introduced. Then some advanced and newest technologies of energy savings and optimal control for EVs, such as the high-efficiency traction motor, intelligent battery management system, regenerative braking with high energy recovery, and the vehicle energy management, will be included and discussed as well as the key results. The detailed contents of this chapter are as follows:

2. Introduction of EVs

2.1. EVs

The transportation sector is the largest consumer of oil and it has grown at a higher rate than any other sector in recent decades [1]. Increases in transportation have caused pollution

emissions because of the utilization of ICEs, and that have consequently caused some environmental problems, which must be prevented to maintain the quality of life. Thus, many governments have developed more stringent standards for the pollution emissions of vehicles. In order to achieve better fuel economy and lower emissions, both academia and automotive industry have conducted research on improving the efficiency of powertrains, developing other energy sources, and changing the concept of the conventional powertrains to EVs including PEVs, HEVs, and FCVs. Among them, PEVs use electric motors for traction and batteries or supercapacitors for energy storage systems. FCVs take the fuel cells as the energy sources, however, the fuel cells do not have the energy recovery function which the batteries and the supercapacitors have. PEVs and FCVs have many outstanding advantages over ICE vehicles such as zero emission, independence from petroleum, higher efficiency, and quiet operation [2]. As a power source, a fuel cell system (FCS) has a relatively slow power response and the ICE or the fuel cell cannot recover the vehicle braking energy. Thus, the size of the FCS or the ICE will be increased if the FCS or the ICE is the only power source in a vehicle. The secondary power source which has a relatively quick power response and can recuperate the braking energy is needed, and a battery or a supercapacitor could be one of the candidates for the secondary power source. Hybrid powertrain structure is the solution of the above requirements. A fuel cell hybrid vehicle (FCHV) or an HEV can provide sufficient power during its acceleration and can recuperate the kinetic or potential energy of the vehicle during braking by the hybridization.

2.2. The state of the art of energy saving and optimal control technologies for EVs and the technical challenges

For the traction motors, the optimization of different machines is still the most important means to pursue higher power density and higher efficiency. In order to reduce the overall weight, volume, and cost, the integrated motor drive becomes more and more popular which integrates the circuit of the charger into other power electronic circuits existing in EVs. In addition to the three-phase AC motors, switched reluctance motor (SRM) has attracted increasing attention recently due to its low cost, simple structure, good controllability, high efficiency, and wide operation range. SRMs have been extensively applied to the electric drive systems of EVs.

For the BMS of EVs, the main and key difficulties are the voltage balance and the battery SOC estimation. The voltage balance is dependent on the accurate estimation of the battery SOC. Thus, the battery SOC estimation is not only for the voltage balance but also for achieving a good energy management result. Currently, the ampere-hour (Ah) model is one of the most widely used methods in this area.

For the RBS, in spite of the significant benefits of RBS, there are still technical challenges. The battery conditions, including the SOC and temperature, affect the energy recovery. When the SOC is too high, the regenerative braking energy may not be fed back to the battery. The hydraulic braking system functions instead of the RBS in such case. Additionally, the hydraulic braking system is reserved in case of failure of the electric braking actuator. Therefore, the hybrid brake system (HBS) that consists of both the hydraulic and the regenerative braking

http://dx.doi.org/10.5772/59420

systems is the main architecture in this area, which is further divided into the parallel type and the series type. The HBS needs an appropriate coordination mechanism between the two subsystems to achieve multi-objectives, i.e., safety, energy efficiency, and brake comfort. Various control methodologies including the rule-based, fuzzy logic-based, robust control-based, and neural network-based approaches have been proposed and investigated in the literature. Nevertheless, the HBS needs further studies due to the model nonlinearity, parameter uncertainty, external disturbances, and the interaction with the driver's operation on the brake pedal. From the point of view of the safety and energy savings, emphasizing the electric braking force is a significant trend in future.

For the energy management of EVs, rule-based energy management strategies are usually used currently because of the simplicity. Other advanced strategies, for example optimal control theory-based energy management strategies, are still on the research step due to several unsolved problems such as lack of the memory for big data saving and low speed of the processor. In addition, the research on the energy management strategies using the prediction of future driving condition is active currently, as the driving route of the vehicle is not fixed in the real-world driving.

3. Electric driving technologies

3.1. Introduction of EV traction motors

The traction motors, working as the heart of powertrains, are the most important key components of modern EVs. Unlike conventional motors, traction motors and drive systems for EVs are under special demands, such as compact structure, light weight, high reliability, high efficiency, low noise, low vibration, wide operating range, and most importantly, low cost. With the harsh requirements, innovative concepts are used to design the EV traction motors, which include the innovations on conventional motor structure, principle, design, performance, and manufacturing technology. In order to achieve high power/torque densities, high reliability, and wide operating range, a lot of new technologies such as water-cooled frame structure, internal oil-cooled stator structure, thin-shell frame, and ultra-short and solid filled-in end-turns will be utilized. Due to the natural disadvantages, such as complicated brush assembly, poor reliability, and the need of maintenance, conventional brushed DC machines are not suitable for larger scale commercial application in vehicle business. Modern vehicles normally use AC machines without brushes, namely, induction machines, switched reluctance machines, and permanent magnet AC machines.

To pursue a high power density of machines, the major task is to increase the peak output torque, rather than the rotating speed, because the speed may be limited by applications and manufacturing technology of the powertrain. The size and weight of machines are mainly related to the peak output torque, not peak output power. The peak torque depends on the saturating level of magnetic path and the current in the winding. Designers have to endlessly optimize the structure of magnetic path to achieve better usage of ferromagnetic materials and search for peak torque with smaller winding current. For the similar heat dissipation condition,

the smaller winding current results in less conductor materials and the ferromagnetic materials surrounding them and consequently leads to less resistance losses in the conductor and less iron losses in the ferromagnetic materials. Hence, the higher power density requires the higher efficiency, while the higher efficiency normally results in the higher power density. Under certain situations, the higher power density can also be achieved with higher current density, which requires promotions on the heat resistance of materials and improvements of heat dissipations. However, such solutions demand for better materials and manufacturing technologies. The total power loss will be the largest in induction machines, smaller in reluctance machines, and the smallest in permanent magnet (PM) machines. The efficiency of the machines will follow the reverse sequence. Thus, the PM machines come with the most potential for higher power density. In fact, the optimization of different machines is still the most important means to pursue higher power density and higher efficiency.

3.2. Electric drive based on integrated technology

Transport electrification has been considered as one of the most promising solutions to the urgent challenges facing our human beings, such as global warming, environmental pollution, energy crisis, and so forth [3]. Most recently, with the advent of the vehicle-to-grid (V2G) technology [4], the gridable EVs that can be directly connected to the utility grid have been expected to function as distributed energy storage system during the parking period, so as to balance the demand and supply of the electricity market in the future. Generally, gridable EVs include battery EVs, plug-in hybrid EVs [5, 6], and range-extended EVs [7].

In contrary to the traditional EVs, the gridable EVs are equipped with plugs and on-board chargers. By connecting the plug to the utility grid, the electrical energy can flow into the on-board batteries through the on-board charger. Moreover, the energy deposited in EVs can also be fed back to power grid when the bi-directional on-board charger is engaged.

In gridable EVs, the high power energy conversion systems are installed, for example, motor drive system, low voltage DC/DC converter, electrical air conditioning system, battery charger system, and grid-connect inverter shown in Figure 1. Many complex power electronics and electrical systems bring the serious challenges from system layout, installation, weight, cooling, electromagnetic compatibility, and cost, etc. The diverse needs for the electromechanical systems of EVs can be satisfied by the development of integrated technology.

In order to reduce the overall weight, volume, and cost, integrated motor drive becomes more and more popular to integrate the circuit of the charger into other power electronic circuits existing in EVs. In the previous publications, the circuits of motor drive and the motor are involved to construct integrated on-board chargers [8, 9]. Due to the neutral point of AC motors, one terminal of AC line can be conveniently connected to the neutral point, and the three-phase windings can function as the couple inductances in the boost converter circuit. However, the boost converter topology requires the input voltage lower than the output voltage. Thus, such kind of integrated charger is more feasible in countries and regions where 110 V AC power is adopted. In order to extend the range of the input voltage, the buck converter has been added to the battery side.

http://dx.doi.org/10.5772/59420

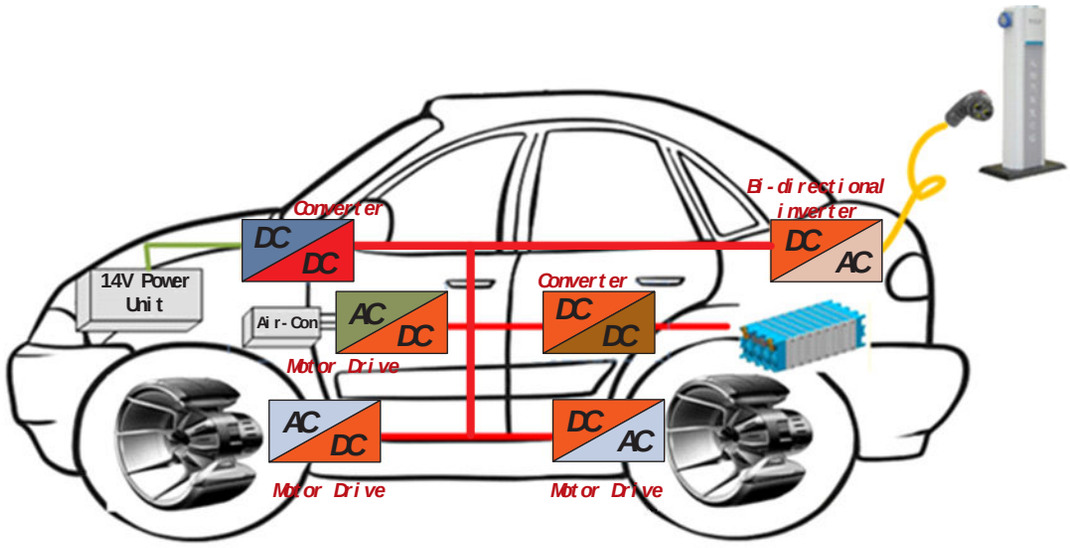

Figure 1. Main electrical energy conversion system in EVs

In addition to the three-phase AC motor, SRM has attracted increasing attention recently due to its low cost, simple structure, good controllability, high efficiency, and wide operation range [10, 11]. SRMs have been extensively applied to the electric drive systems of EVs. The purpose of this study is to propose a novel integrated SRM drive with the bi-directional inverter to reduce the cost, volume, and weight for EV applications.

3.3. Integrated technology of switched reluctance motor drive

3.3.1. Conventional SRM and its converter

SRMs, which are non-rare earth permanent magnet motor, have been recognized as the considerable candidates for EV and HEV applications. It has salient poles on both rotor and stator, but only the stator carries windings. The torque is produced by the alignment tendency of poles. The rotor will shift to a position where the inductance of the excited winding is maximized. Therefore, the advantages of SRMs can be summarized as simple construction, low manufacturing cost, and outstanding torque characteristics. The structure of SRMs is shown in Figure 2.

When the rotor position enters into inductance increasing region, this phase winding is injected with the phase current. SR motor operates at motoring mode and produces positive torque. Contrarily, SR motor operates at regeneration mode and produces negative torque. Motoring and regeneration modes of SRM are shown in Figure 3.

For EV applications, the conventional SRM drive uses a battery source and a large capacitor in the front-end as shown in Figure 4. This capacitor helps the battery to keep a steady DC-link voltage, acting as a low-pass filter. Another function of DC-link capacitor is to store the magnetic field energy when the SR motor is demagnetized.

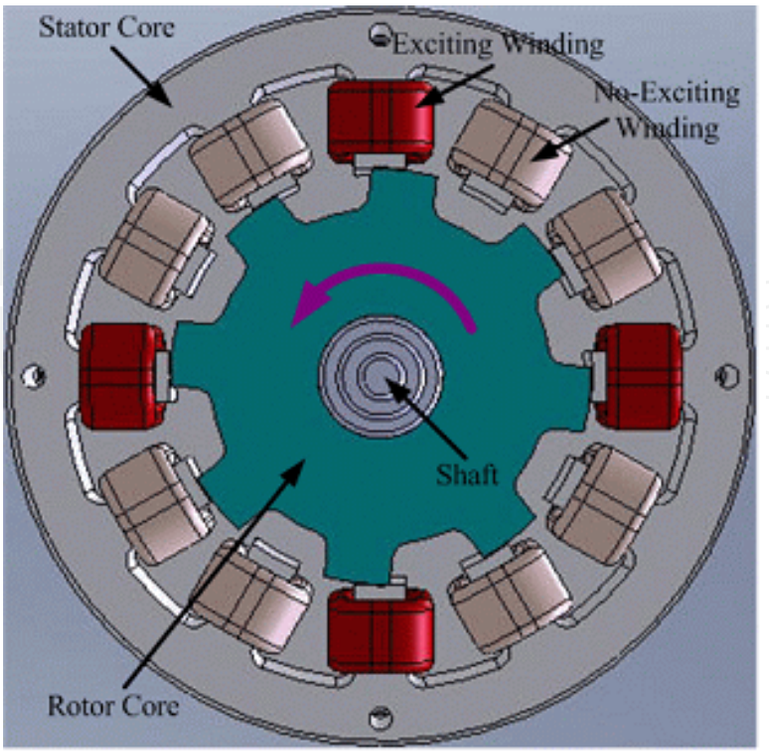

Figure 2. Excited phase winding in 12/8 3-phase SRM

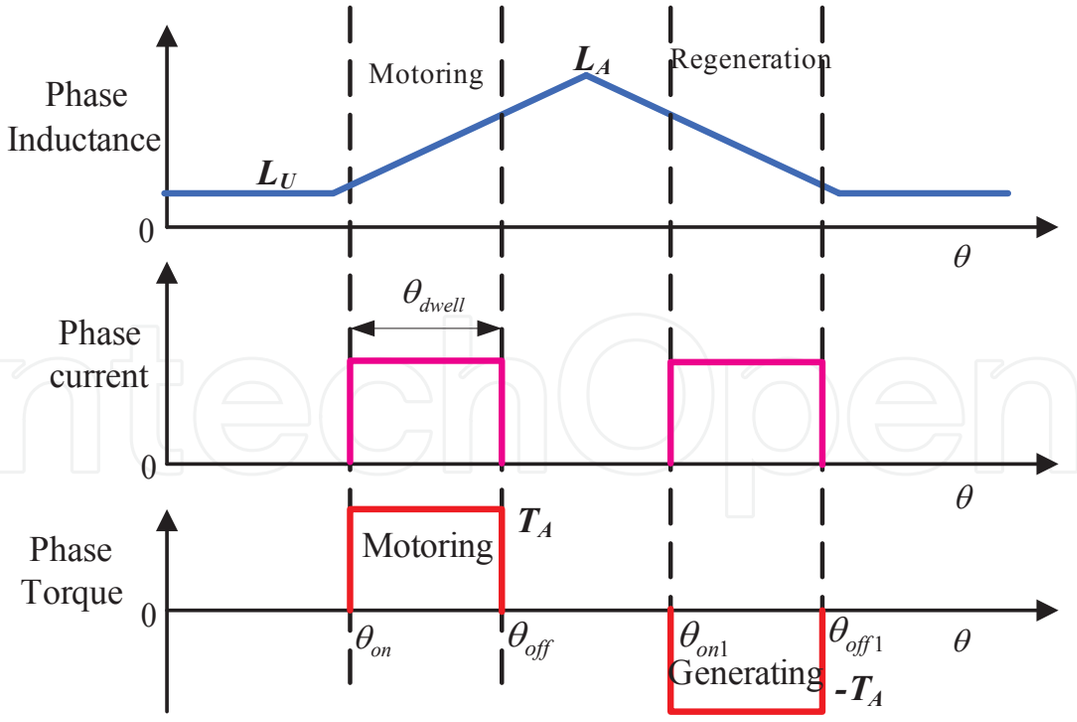

Figure 3. Motoring and regeneration modes of SRM

http://dx.doi.org/10.5772/59420

The asymmetric bridge converter consists of two power switches and two diodes per phase, which can support independent control of each phase and handle phase overlap. The asymmetric converter has three modes, which are defined as magnetization mode, freewheeling mode, and demagnetization mode as shown in Figure 4 (b-d).

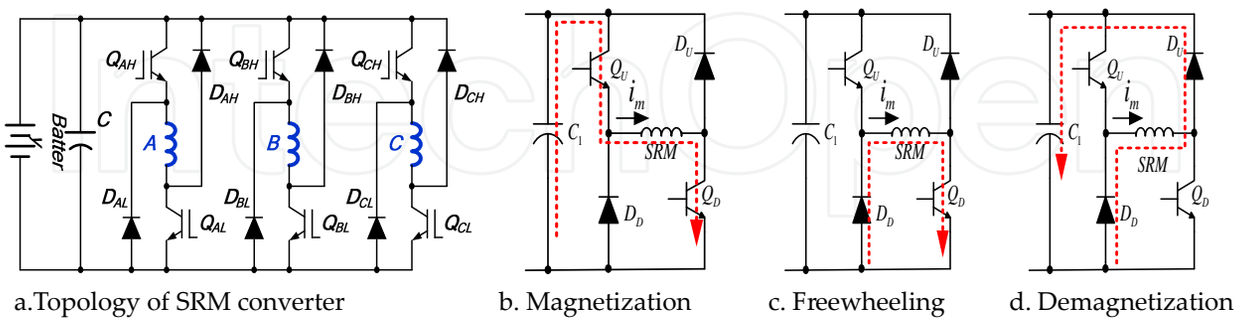

Figure 4. Conventional 3-phase SRM drive and its operation modes

3.3.2. Integrated switched reluctance motor converter

In the conventional EV application, the on-board battery charge and the grid-connect inverter are independent devices. To reduce the size, weight, and cost, the integrated SRM drive with the bi-directional inverter is introduced [12]. The integrated converter can be operated as: SRM drive, battery charger, and grid-connect inverter. In order to improve the coefficient of utilization, the power switches, inductors, capacitors, and controller are multiplexed in the same circuit. For city vehicle application, the operation of driving mode, battery charging mode, and grid-connect mode can be divided by Time-Division Multiplexing (TDM) method. The integrated drive system can be served the activity plan of daily as shown in Figure5. The integrated system can be seamless transferred to each application. Of course, more complicated case can be supported by this method.

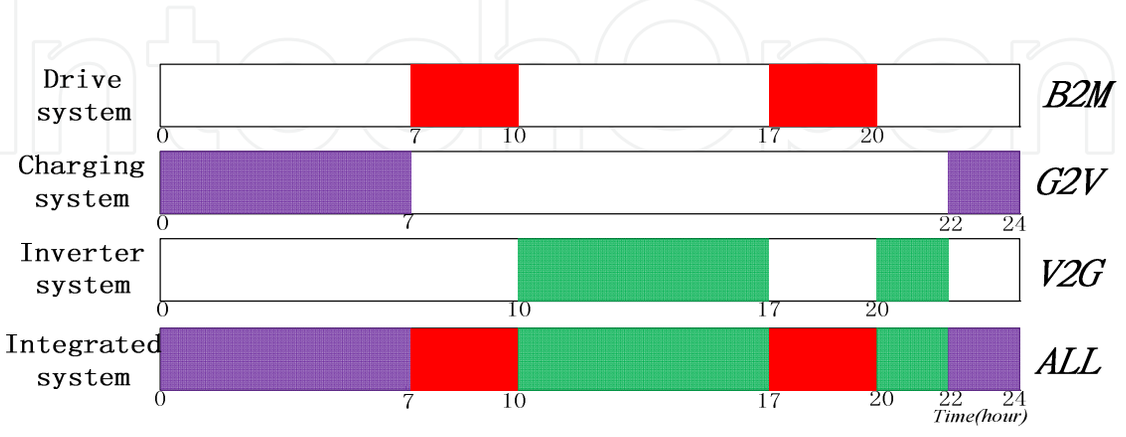

Figure 5. The activity plan of different application in working day

The battery charger is a device used to put grid energy into the battery by forcing an electric current through it. It consists of the rectifier, the boost converter, and the buck converter. The grid connect inverter is a device used to put battery energy into the grid. It is made up of the boost converter and inverter bridge. Due to the power factor requirement, the power factor correction is required to perform. The topology of three circuits is shown in Figure 6. In order to build the integrated motor drive, all the functions of the three devices should be included.

A novel integrated SRM drive with the bi-directional inverter is introduced in Figure 7 [12]. Compared with the conventional asymmetric converter, the two lines from the plug outlet are connected to the cathode of the lower diode in phase A and B. A relay is added between the switch Q_{CH1} and the switch Q_{CH2} to divide the voltage stage of DC-link and battery. In order to reconstruct the bi-directional converter, two free-wheeling diodes of phase C's are replaced by two power switches with parallel protection diodes.

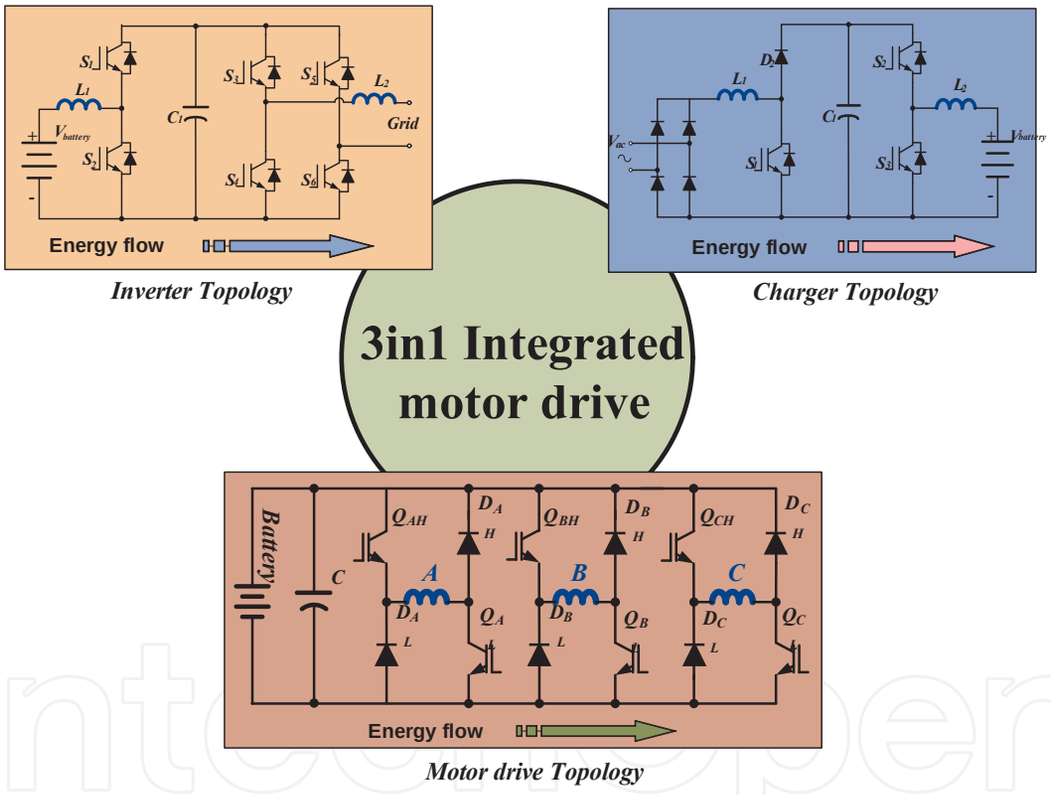

Figure 6. The circuit topology of motor drive, charger, and inverter

Obviously, two stages of the bi-directional converter are suitable for the battery charger application due to the wide range of the battery voltage. The bulk capacitor of the motor drive is designed to separate two parts and serve two independent voltage stages. In the driving mode, the two capacitors are paralleled to increase the capacitance value. In the bi-directional converter mode, the two capacitors are divided: one is for the boost voltage stage, and the other is for the battery voltage stage. In the battery charger mode, the relay is opened and the proposed integrated SRM drive is constructed by the bridgeless power factor correction (PFC)

http://dx.doi.org/10.5772/59420

front-end and the buck-boost converter. The bridgeless PFC front-end can improve the efficiency of AC-DC conversion. The key point of this integrated SRM drive is that it applies the motor winding as the boost inductance and the buck inductance [12]. In the grid-connected inverter mode, the relay is similarly opened. The bridgeless PFC frond-end is operated as a single phase inverter, and the full bridge converter of the phase C is run as a boost converter in the opposite direction [12].

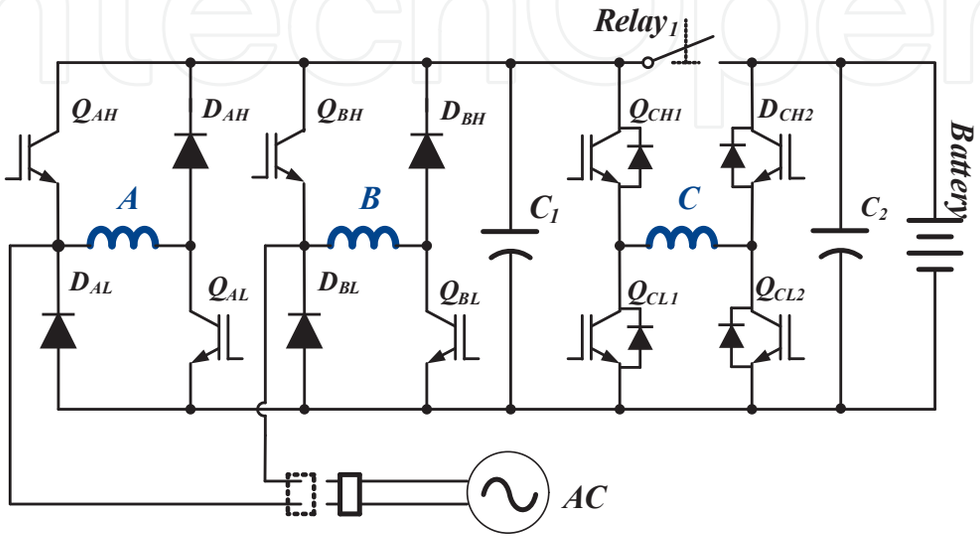

Figure 7. A novel integrated SRM drive with the bi-directional converter

3.3.3. Control strategy of the integrated motor drive

For the normal inverter, the inductance is only like a static transformer. However, in the novel integrated drive system, the inductance of the integrated inverter is related to the phase winding of SRM, which varies according to the rotor position and phase current. In this application, the phase inductance is limited by the primary characteristic of the SRM drive. Thus, three problems can be found: the first is that the inductance of the SRM is changed by the rotor position; the second is that the relative space angle between phase windings is 120 electrical degrees; and the last is that the phase inductance has effects of magnetic saturation.

In the motor driving mode, the rotor performs the rotational motion according to the instructions. However, unlike the driving mode, the rotor position of the battery charging mode and the grid-connect mode prefers not to rotate. The rotation and vibration only increase the loss of energy conversion. Two questions appear: how to fix the rotor at still and how to find the suitable position.

For the fixed position, two methods can be selected: the mechanical brake method and the zero torque control method [11]. For the mechanical method, the rotor will be locked by the mechanical structure. The motor torque will be counteracted, but the mechanical components increase the cost and space. Due to satisfy the power factor correction and battery charging,

the sine wave current is injected in the phase A or B, and phase C is flown in the direct current. Therefore, the zero torque control method cannot be applied in this converter topology [13]. Thus, the mechanical method is used, and the advantage is that the rotor position is easy to set to any position.

For finding the suitable rotor position, the aligned position of the phase A is defined as zero. Ignoring the influence of mutual inductance, the inductance of the SRM is a periodic function of the rotor position, and it can be simplified and expressed using Fourier series as follows:

$$L(\theta, i) = \sum_{n=0}^{\infty} L_n(i)\cos(n\theta) \qquad (n = 0,1,2...) \tag{1}$$

where *Ln* (i) is the amplitude of the Fourier components, whereas θ_A, θ_B, and θ_C are electrical degrees of each phase. In a three phase SRM, the axes of the three-phase windings are spaced 120° electrical degrees from one another, that is

$$\theta_A = \theta \tag{2}$$

$$\theta_C = \theta + 2\pi/3 \tag{3}$$

$$\theta_B = \theta + 4\pi/3 \tag{4}$$

For the bridgeless PFC front-end circuit, a boost inductor is needed to boost-up the DC-link voltage. However, in the novel integrated drive system, the winding of phase A or B is alternated to replace the boost inductor in the different half-cycle of sinusoidal voltage. Obviously, the inductor of the phase A and B should be equal in value to make the circuit symmetrically. Therefore, the charging position of the novel integrated system must meet the inductor requirement.

$$L(\theta_A, i) = L(\theta_B, i) \tag{5}$$

The inductance of the phase A and B can be calculated from (1), (4), and (5):

$$\theta_A = -\frac{2\pi}{3} + k\pi, \qquad (k = 0,1,2..) \tag{6}$$

So, meet the conditions in case of rotor position is

http://dx.doi.org/10.5772/59420

$$\theta_A = \frac{\pi}{3}, or \quad \theta_A = \frac{4\pi}{3}. \tag{7}$$

In both cases, the difference between the inductance of the phase A and B is clearly indicated in Figure 8. The inductance of the phase A and B at π/3 is higher than that at 4π/3. However, the inductance of the phase C reaches the maximum value at 4π/3 and the minimum value at π/3. The selection of the charging position should be decided by the real application. Due to the phase C winding used by DC/DC converter, the inductance of the phase C will affect the dynamic response ability.

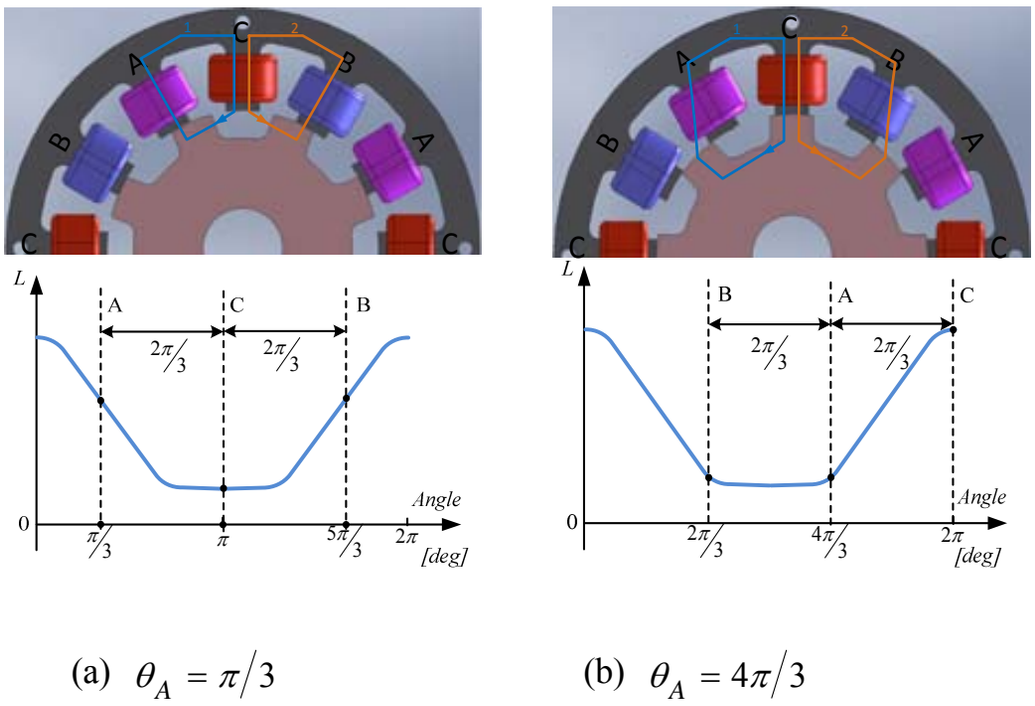

(a) $\theta_A = \pi/3$ (b) $\theta_A = 4\pi/3$

Figure 8. Rotor position of phase A in the bi-directional inverter mode

The block diagram of the novel integrated SRM drive system is shown in Figure 9. In the driving mode, the battery supplies the stored energy to drive SR motor, and the power flow is through the battery, integrated converter, and SR motor. When the outlet is connected to the grid, the vehicle management system should decide operation mode of the integrated drive system. If charging mode is executed, the asymmetric converter of the phase A and B is operated as a bridgeless PFC converter to meet the requirement of the PFC and DC-link voltage. And the full bridge converter of the phase C is implemented as a buck converter to manage the battery charging strategy. The power flow is followed the grid, SR motor, proposed converter, and the battery.

Due to the topology of the bridgeless front-end, the positive half cycle of the line current is injected into the winding of the phase A, and the negative half cycle of the line current is

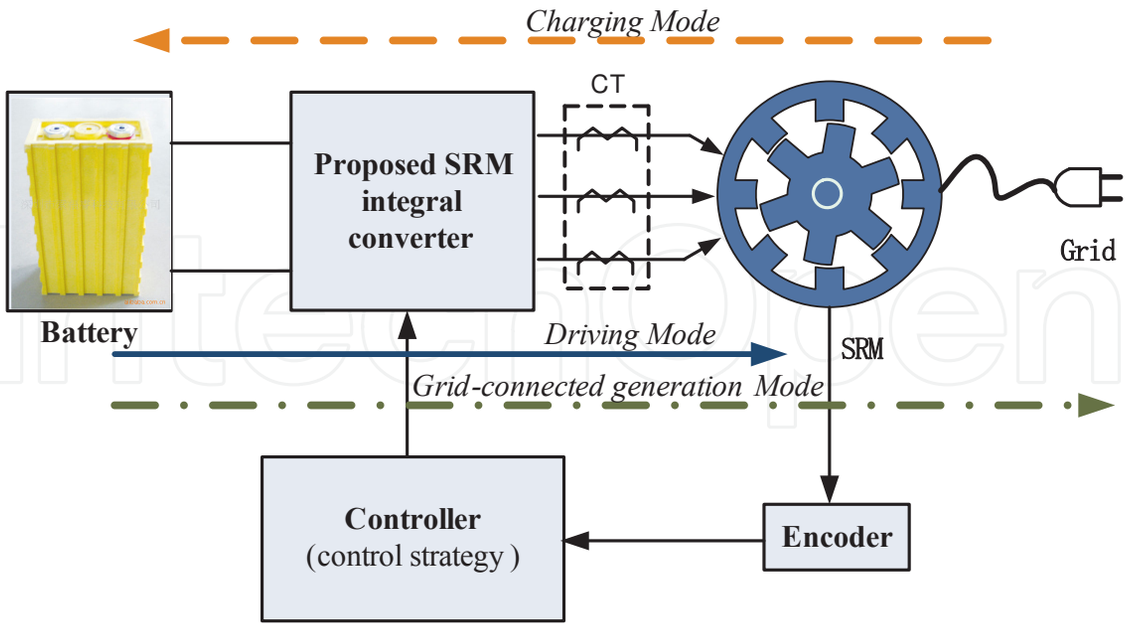

Figure 9. Block diagram of the integrated system

injected into the winding of the phase B. However, the input line current waveform is also sinusoidal. At the rotor position of 4π/3, the inductance of the phase C reaches the maximum value and the torque of the phase C is zero. Because the phase A and B are conducted in turn, the total torque of the rotor is not equal to zero in Figure 10. The power factor of 220Vac input is 0.99.

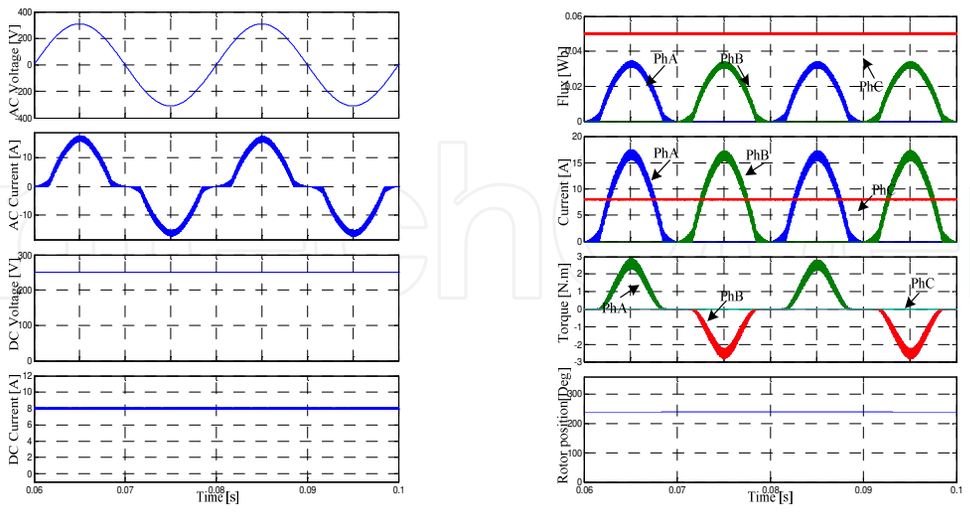

(a) Voltage and current (220[*Vac*]) (b) Current, flux and torque (220[*Vac*])

Figure 10. Simulation results of novel integrated system in charging function (220V)

http://dx.doi.org/10.5772/59420

If the inverter mode is carried out, the quadrant DC/DC converter of the phase C is implemented as a boost converter which meets the DC-link voltage requirement. The asymmetric converters of the phase A and B are acted as the inverter bridges. The power flow passes the battery, converter, SR motor, and the grid.

In the inverter function (Figure 11), the current of the phase C is the reverse direction of charging function's. Thus, the phase current and flux of the phase C are negative. Since the current of the phase A and B is unidirectional, the flux of them is positive. For the battery side, the battery discharges the energy to the DC-link. The current and voltage of power grid have 180 degrees.

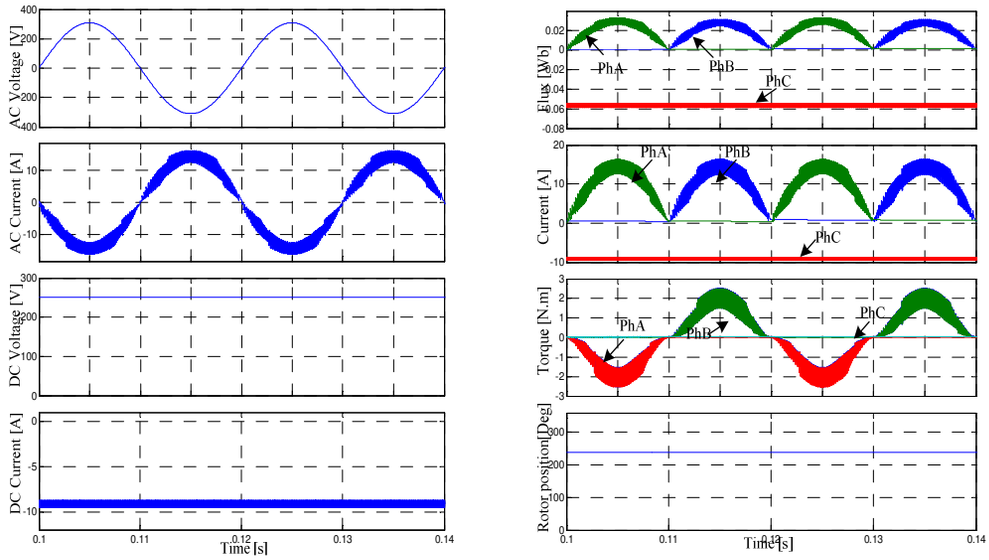

(a) Voltage and current(220V) (b) Current, flux and torque(220V)

Figure 11. Simulation result of proposed integrated system in inverter function (220V)

4. Advanced battery management technologies

4.1. Introduction of battery management system (BMS)

The lithium-ion battery has attracted special attention for HEVs and EVs owing to its advantages of high specific power, high energy density, no memory effect, and long durability. What is more, research is yielding a series of improvements to traditional manufacturing technology focusing on power density and intrinsic safety of battery.

A BMS is an important means for raising the intrinsic safety and durability of batteries. The main parameters of the batteries are monitored with the BMS including the voltage, current, temperature, and also the leakage detection and SOC & state of health (SOH) condition. The maximum mileage and the charging control algorithm can be achieved based on the battery

voltage, current, and temperature under the maximum output power control algorithm. The real-time communication is achieved between the CAN bus interface and the vehicle master controller, motor controller, energy control system, and automotive display systems. The BMS is a bridge between the battery and drivers, and it plays a critical role for the EV performance. The diagram of the BMS is shown as Figure 12.

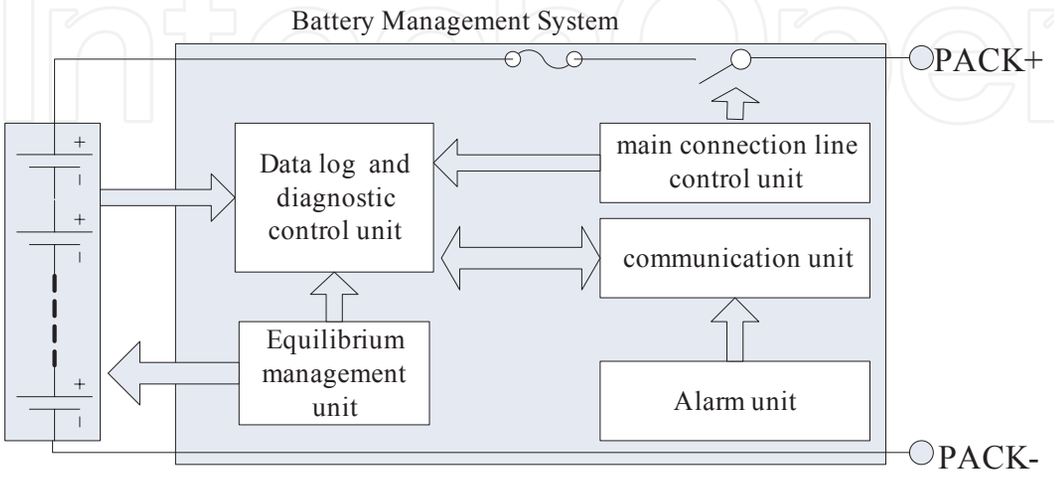

Figure 12. Diagram of the BMS

4.2. SOC estimation of Lithium-ion batteries

Many ways of SOC estimation have been proposed in the literature [14]. According to the main detection parameters, they are classified into voltage model, resistance model, current model, and intelligent algorithm model [15]. The open circuit voltage (OCV) provides the useful information on the intrinsic characteristics of the battery and it declines proportionately with the energy expenditure [16]. However, it does not apply to frequent repeated conditions of charge/ discharge. Moreover, this similarly situation also occurs in the resistance model. Ah model is one of the most widely used methods, and it is an iterative algorithm of dynamic current with time integral. The main drawback is the initial SOC (SOC0) cannot be estimated. Additionally, the intelligent algorithm model, such as Kalman filter model, Extended Kalman filter model, and Artificial neural network model, is highly dependent on the quantity of battery model and input variables, which greatly influences the accuracy and computational complexity. The hybrid model of OCV model and Ah model is considered to be easy to accomplish. Additionally, it is easily implemented in EVs and it needs uncomplicated hardware.

4.2.1. Definition of terms related to SOC

Accordingly, when a battery is in discharging step, the formula to calculate SOC as the ratio of releasable capacity, $Q_{releasable}$, relative to the rated capacity, Q_{rated}, during the profiles is as follows:

http://dx.doi.org/10.5772/59420

$$SOC = \frac{Q_{releasable}}{Q_{rated}} \times 100\% = (1 - \frac{Q_{consumption}}{Q_{rated}}) \times 100\% \tag{8}$$

If the discharging step is not from the rated energy, the Ah model of SOC estimation could be expressed as (9) and shown as Figure 13. The real time SOC estimation (SOC (t)) is equal to the plus of the initial SOC (SOC0) and the ration of the consumption capacity with the rated capacity in an operating period τ. I is positive for discharging and negative for charging. To enhance the accuracy of SOC estimation, the energy efficiency denoted as η is considered.

$$SOC(t) = SOC_0 + \Delta SOC = SOC_0 + \eta \frac{-\int_{t_0}^{t_0+\tau} Idt}{Q_{rated}} \times 100\% \tag{9}$$

4.2.2. The function of OCV to SOC0

The lithium-ion battery used in the investigation is $LiFePO_4$/graphite battery. A $LiFePO_4$ battery with nominal voltage of 3.65 V and nominal capacity of 20 Ah is selected.

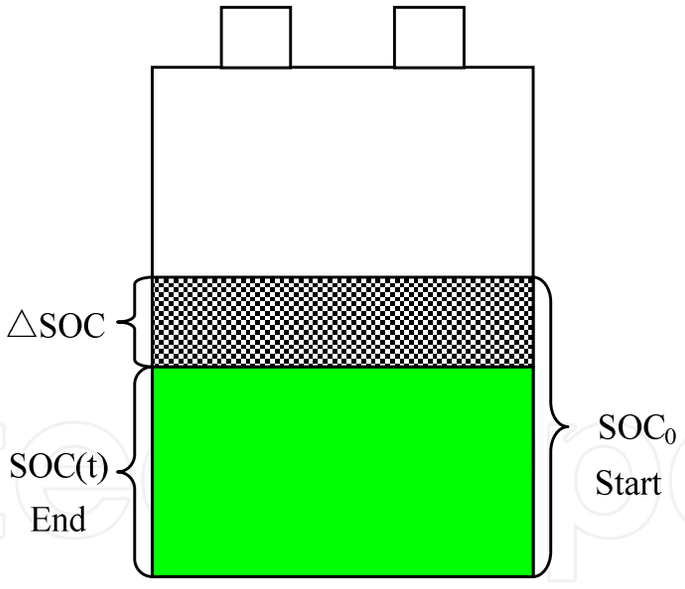

Figure 13. Diagram of relative locations of the initial SOC (SOC0), real time SOC (SOC (t)), and the ration of energy discharged ΔSOC

The OCV is the equilibrium potential difference of an electrode, which depends on the temperature and the amount of active material left in the electrolyte. The OCV can be calculated by Nernst equation [17]. However, the measured voltage at the breaking of the current cannot be denoted as OCV because of the presence of polarization and the relaxation of solid particles. In fact, after the short discharge, the terminal voltage is gradually increased due to relaxation

of over potentials and eventually leveled off to an equilibrium potential. Figure 14 illustrates the OCV as a function of SOC after discharging at a room temperature. The verification experiment is conducted to calculate the accuracy of the above estimation method of OCV (see the circles in Figure 14).

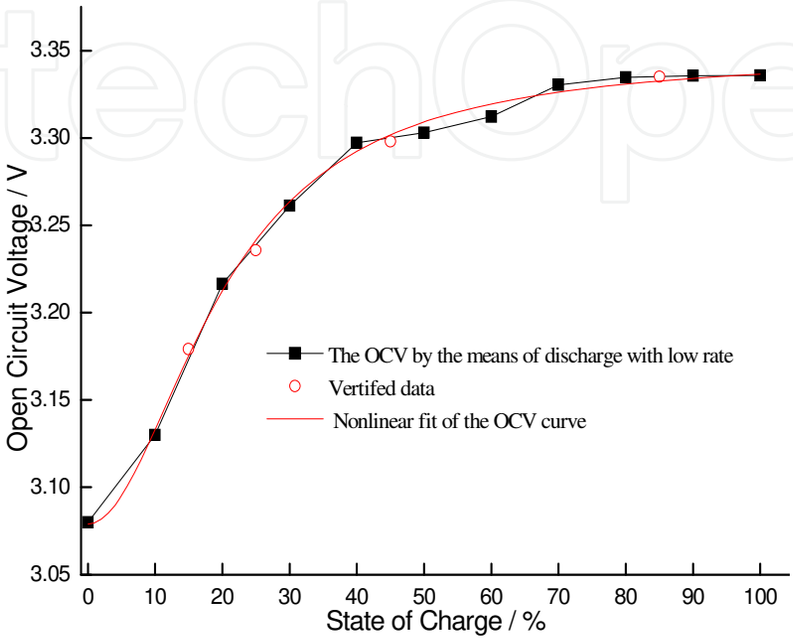

Figure 14. The comparison profiles of the measured voltage and the nonlinear fit

In this study, the quantitative relationship between the SOC and OCV as the logistic function (equation (10)) is proposed. The values of b and p are 20.12155 and 1.97038, respectively, and the correlation coefficient of the fit is 0.997.

$$U = \frac{U(SOC0\%) - U(SOC100\%)}{1 + (SOC_0 / b)^p} + U(SOC100\%) \tag{10}$$

4.2.3. The function of temperature to SOC0

To mitigate the estimation error, the following technique is used in this work. At a certain temperature, the relationship between SOC0 and OCV is obtained and can be established using nonlinear function. dV0 /dT is proportional to the entropy of reaction by the relation dV0 / dT=ΔS/nF, where n is the number of electrons passed in the reaction and F is Faraday's constant, and reflects the influence of the incremental lithium atoms on the ordering of lithium-ion in the host lattice [18].

The battery is discharged to a designed SOC and kept to a temperature of 30°C for 20 hours. This is to impel the degradations of diffusion and migrant to obtain a steady voltage. The

http://dx.doi.org/10.5772/59420

temperature experiments focus on the changes of OCV under different ambient temperature conditions of 3°C, 15°C, 25°C, 35°C, and 45°C for 0.5h [19]. The result is shown in Figure 15. The results reveal that the temperature affects the changes of OCV. To reduce the error of temperature upon the SOC0 estimation, the voltage is calculated according to a unified energy unit under a constant temperature, which selects 25°C as a base.

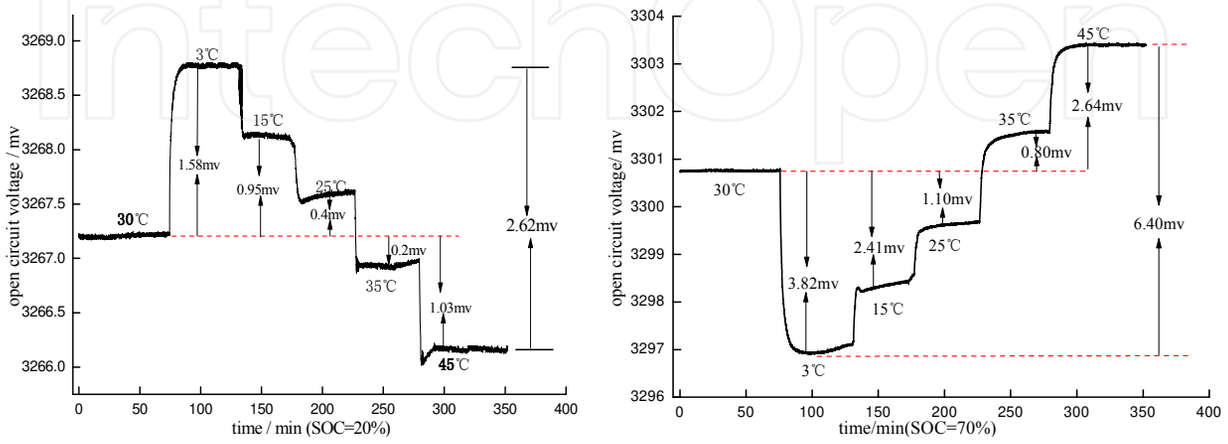

Figure 15. OCV under different temperature (the first and the second subplots respectively correspond to the cases in which SOC=20% and SOC=70%)

Through the above analysis, we can see that the temperature and resting time have significant impacts on the SOC0 estimation. In the present study, the quantitative relationship (equation (11)) exhibits the functions of terminal voltage u, resting time t, and temperature T to SOC0 based on the theory above.

$$SOC_0 = f_3(\Delta t)\exp\frac{1}{f_4(\Delta t)}\left(\frac{f_2(\Delta t)}{u - f_1(\Delta t) - \Delta u(T)} - 1\right) \tag{11}$$

Meanwhile, the temperature correction factor Δu (T), which reflects the influence of the temperature variation on the OCV, is also considered when estimating SOC0.

4.3. Energy Efficiency for intermittent charging-discharging

In order to fully explore the effect of thermal characteristics of lithium-ion battery on the energy efficiency under the continuous process of charging and discharging, the energy balance model under the heat generation behavior is investigated. The energy balance for batteries consists of chemical reactions, ionic mixing, electrical work, and heat transfer with surroundings [20]. Assuming that the temperature distribution in the battery is uniform and the enthalpy of ionic mixing and the radiation between the battery and the environment are neglected, the energy balance function can be written as:

$$q = I^2R + I(\eta + T\frac{\partial V_0}{\partial T}) + MC_p\frac{dT}{dt} \tag{12}$$

$$\eta = V_0 - V \tag{13}$$

Where V0 is the OCV, V is the terminal voltage, q is the heat transfer rate between battery and the surrounding environment, I is the current, R is the resistance, η is the over potential, $IT^{\partial V_0}/_{\partial T}$ is the reversible heat, and Cp is the heat capacity of the battery.

In the charge/discharge cases, we are interested in evaluating how much energy is lost due to the thermal characteristics as a function of internal feature in the battery. If the irreversible reaction energy is ignored and considering the battery back to the initial state after the cycle, the energy balance function can be expressed as follows:

$$e_{charge} + TI_1\frac{\partial V_0}{\partial T} = I_1^2R + \eta I_1 + e_{discharge} + TI_2\frac{\partial V_0}{\partial T} + I_2^2R + \eta I_2 \tag{14}$$

To create an energy efficiency model for the charge/discharge cases, we similarly ask what percent of energy loss E_{loss} will be existed in a battery if the battery is charged or discharged at a given current I and a variable power P. The relative definitions of power P, energy loss E_{loss}, and energy stored E_{charge} or discharged $E_{discharge}$ can be visualized in Figure 16.

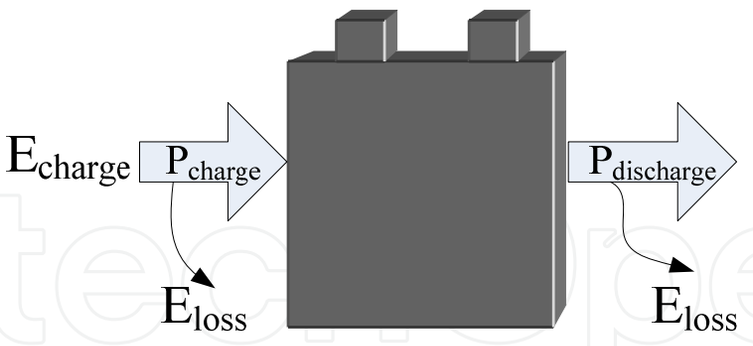

Figure 16. Diagram of relative locations in charge/discharge cases

In the process of charging and discharging, the energy lost caused by the battery thermal characteristics can be written as follows:

$$\begin{aligned}\Delta E &= E_{charge} - E_{discharge} \\ &= \int_0^{t_1}(I_1^2R + \eta I_1 - TI_1\frac{\partial V_0}{\partial T})dt + \int_0^{t_2}(TI_2\frac{\partial V_0}{\partial T} + I_2^2R + \eta I_2)dt\end{aligned} \tag{15}$$

http://dx.doi.org/10.5772/59420

By using the above function, the energy efficiency of the battery, which is dependent on the thermal feature during constant charge/discharge cycles, is determined by the following:

$$Eff = \left(1 - \frac{\Delta E}{\int_0^{t_1} P_{charge} dt + \int_0^{t_2} P_{discharge} dt}\right) \times 100\% \tag{16}$$

The main parameters of the energy efficiency, resistance, and entropy change coefficient can be determined by experiments. The experiments mainly focus on the thermal characteristics of the lithium-ion battery and the analysis of their effect on the energy efficiency under different depth of discharge (DOD) values, as shown in Table 1.

DOD	SOC	Current (charge)	Current (discharge)
20	40-60	0.3C	0.3C,0.5C,1C
40	30-70	0.3C	0.3C,0.5C,1C
60	20-80	0.3C	0.3C,0.5C,1C
80	10-90	0.3C	0.3C,0.5C,1C

Table 1. Battery test cycle under different DOD values

The experimental results are as follows:

i. Resistance

The discharge test at constant current is performed in the experimental setup and a few representatives are selected at 25°C as shown in Figure 17. The results of the resistance obtained for the SOC values are shown in Figure 17.

ii. Entropy change

Regarding entropy change, there have been many investigations and it is another factor contributing to heat generation in the energy balance. In general, the entropy change ΔS can be estimated from the temperature gradient of OCV, dV0 /dT. dV0 /dT is proportional to the entropy of reaction by the relation $dV_0/dT=\Delta S/nF$, where n is the number of electrons passed in the reaction and F is Faraday's constant, and reflects the influence of the incremental lithium atoms on the ordering of lithium-ion in the host lattice [18].

The entropy change of the lithium-ion battery is positive in the SOC regions of 30%-90%. This means that the thermal behavior of the battery is mainly endothermic during the discharge cycle even if there is no over-potential loss. Different entropy change under different temperature cycle is resulted from the phase change of active material, as shown in Figure 18.

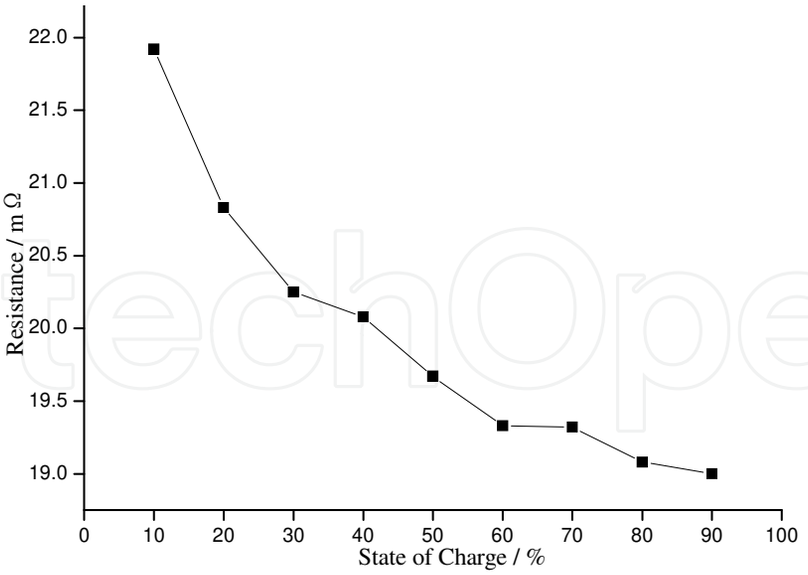

Figure 17. Resistance as a function of SOC

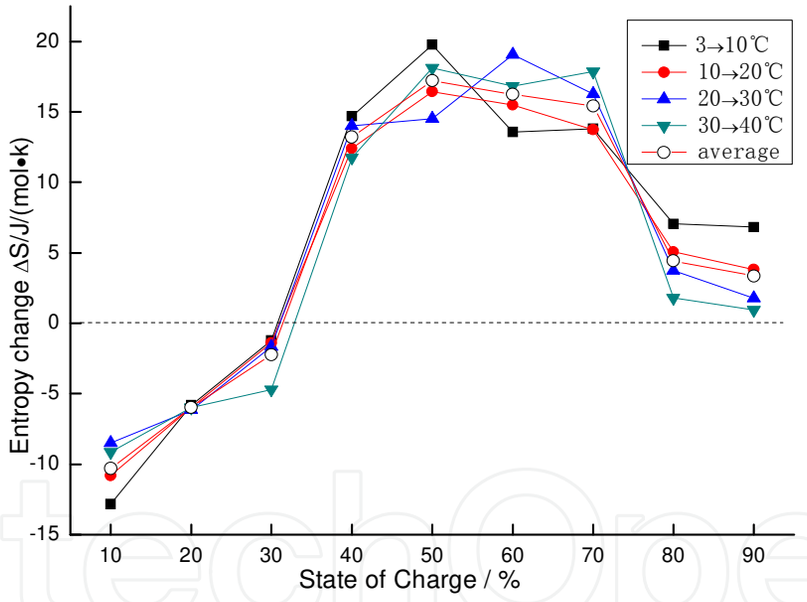

Figure 18. Entropy change for SOC and temperature

iii. Energy efficiency

The battery energy efficiency under the process of shallow charge/discharge is influenced by two factors: (1) External influence factor, such as the DOD, the ambient temperature, and the battery temperature. (2) The energy loss caused by the self-performance, for example, the increasing of resistance, the change of over-potential and the entropy. The above factors cause the energy loss and eventually reduce the battery energy efficiency.

http://dx.doi.org/10.5772/59420

In order to evaluate the contribution of thermal characteristics to the energy efficiency, we explore the effect under discharge and charge process by plotting the energy efficiency as a function of the DOD as shown in Figure 19. By examining the energy loss, we can determine the influence of the heat generation on the battery energy efficiency. The effects of the DOD, current rate, and temperature on energy loss are explored under different discharging interval. The results are shown in Figure 19.

The result of correlation analysis shows that there is a parabola relationship between energy efficiency and depth of discharge under the constant current rate. In addition, the lower the current rate, the higher the energy efficiency. It should be pointed out that the intercept for the minimum energy efficiency at 60% DOD reaches 85.7% at 1C. This may be related to the active material utilization at the above DOD (SOC 20%-80%).

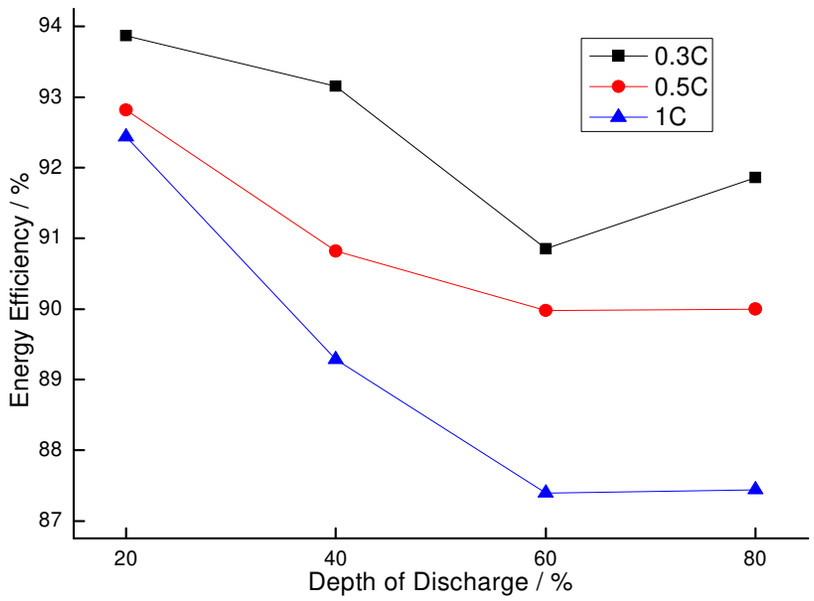

Figure 19. Energy efficiency versus DOD for lithium-ion cells

5. Advanced Regenerative Braking System (RBS) of EVs

5.1. Introduction of RBS

RBS converts part of the mechanical energy into electric energy during braking. The drive motor functions as a generator to provide the brake torque when the vehicle brakes. The potential energy, e.g., the kinetic energy, is converted into electric energy that is then stored in an energy storage system (ESS), e.g., power battery pack, supercapacitor or their combination. When a vehicle starts or accelerates, the drive motor receives the electric energy from ESS to propel vehicle. Utilizing such energy consumption-recycling mechanism, EV recycles a significant amount of energy that is consumed in conventional vehicles [21]. The total energy efficiency and the drive range are thus improved. Recent studies indicate that the energy

savings are completed from 8% to 25% of the total energy use [22-24], depending on the drive cycles and RBS performance. Additionally, the electric brake force generated from the motor is superior to the frictional brake force from the hydraulic brake actuator in terms of precision, accuracy and bandwidth for the torque control and measurement [25].

Maintaining brake safety under various braking conditions is the primary consideration when designing a vehicle brake system. The commercialized EVs/HEVs that utilize RBS still reserve the conventional hydraulic brake device in case of possible failure of the RBS. Another reason for employing the hydraulic brake is the rechargeable capacity of power battery pack. For example, when the SOC is high, the regenerative electric energy may not be fed into the battery, and thus the regenerative brake does not function. In this case, the conventional hydraulic brake is required to provide the brake force alone. The brake system with both the hydraulic brake and regenerative brake is the HBS, which has two architectures, i.e., parallel and series architectures [26]. In parallel braking architecture, both the regenerative torque and the friction torque are exerted on the same drive axle directly, while series braking allows independent modulation of the hydraulic brake torque of each axle according to the regenerative torque, and thus more kinetic energy can be recovered potentially than that with parallel braking.

Controlling the RBS involves multiple objectives, e.g., the total efficiency, brake safety, and comfort. As a RBS is an uncertainty system with parameter perturbation, strong nonlinearity and uncertain external disturbances, the classical control methods that adopt the rule based strategies [27, 28] are ineffective to guarantee the performance. Hence, researchers have studied and proposed advanced methodologies on the RBS control in the literature recently, including the fuzzy control strategies [29, 30], H∞ control [31], and neural network approaches [32]. The studies mostly focused on improving the energy recovery performance based on common factors. However, the vehicle drive safety and ride comfort, which are strongly influenced by the braking performance due to various uncontrollable phenomena by the driver's brake pedal operations [33], need sufficient considerations in the RBS control.

5.2. Regenerative Braking Control Design Based on Fuzzy Control (RBS-FC)

We propose a control methodology based on fuzzy logic for series RBS architecture to facilitate EV's energy-savings and brake safety. The RBS control aims at: 1) preventing wheel's excessive slip and lock via brake torque distribution between the front and rear axles; 2) achieving nearly the optimal regenerative efficiency under normal brake condition.

5.2.1. Braking Force Distribution

The total vehicle brake force F_{car} that is estimated via vehicle acceleration α_{car}, consists of the front brake force F_f and the rear brake force F_r exerted on the front and rear wheels, respectively, which is shown in (17) and the first subplot of Figure 20, where M is the total vehicle mass. However, the load movement during braking may induce wheel lock and the consequent vehicle instability using average torque distribution between the front and rear wheels. Therefore, RBS needs appropriate brake torque distribution law to ensure the braking safety.

http://dx.doi.org/10.5772/59420

$$F_{car} = M \cdot \alpha_{car} = F_f + F_r \tag{17}$$

The ideal distribution curve is represented in (18) and the second subplot of Figure 20, where the symbols are indicated in the first subplot of Figure 20. When RBS control distributes the brake forces to the front and rear axles according to the ideal curve at each friction coefficient, the front and rear wheels do not lock simultaneously. The vehicle handling and stability are thus maintained.

$$F_r = \frac{1}{2}\left[\frac{G}{h_g}\sqrt{b^2 + \frac{4h_g L}{G}F_f} - \left(\frac{Gb}{h_g} + 2F_f\right)\right] \tag{18}$$

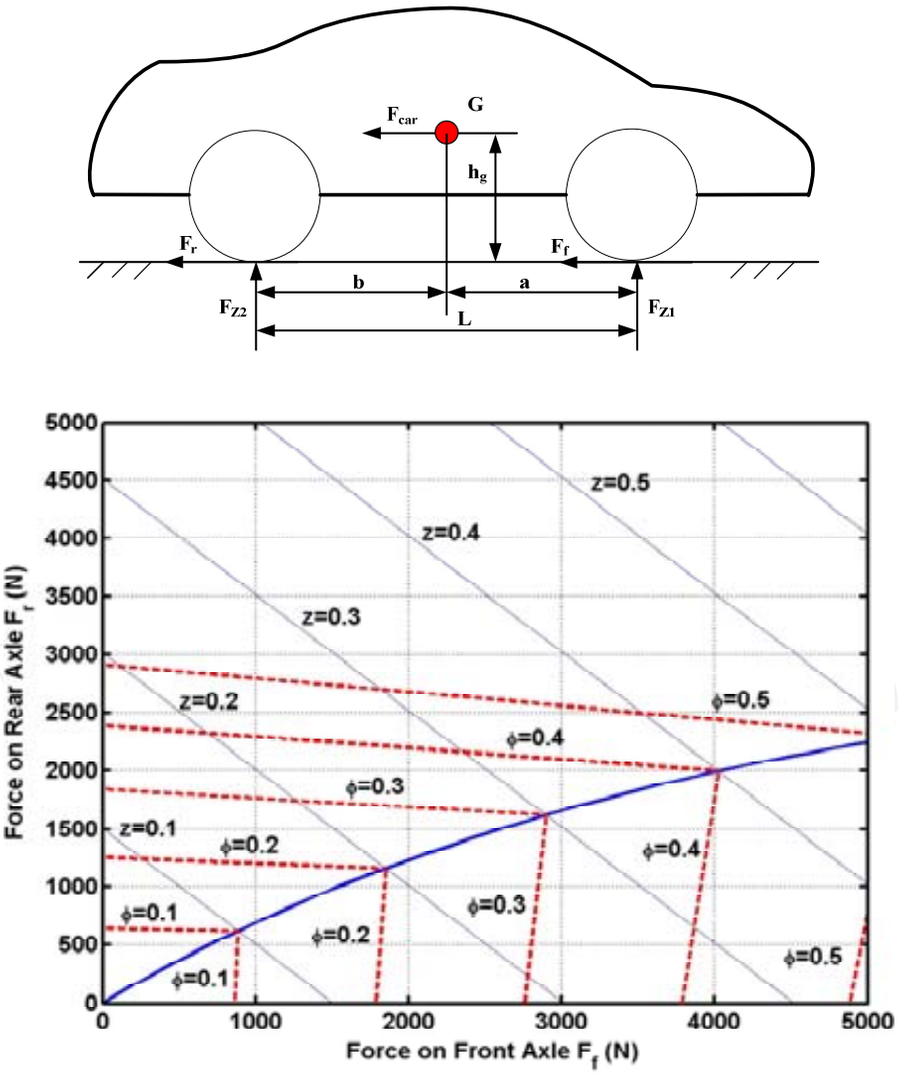

Figure 20. Vehicle braking dynamics on flat road and the ideal distribution curve

5.2.2. RBS based on Fuzzy Control (RBS-FC)

Vehicle speed and the driver's brake force command have large impacts on brake safety. The battery limitations including the battery capacity and the maximum permissible charging current protect the battery cell from damage. The capacity of the batteries is indicated with battery SOC. The maximum permissible charging current is a function of battery capacity Q, battery temperature T, battery SOC, and battery SOH, i.e., $I = f(Q, T, SOC, SOH)$. SOH is hard to determine and has little direct impact on calculating the maximum permissible charging current. Therefore, we only take SOC and battery temperature into consideration here.

The RBS-FC that uses a Takagi-Sugeno model is shown in Figure 21. There are four inputs including battery temperature, SOC, vehicle speed and driver's brake force command. The output is the regenerative brake force. The controller obtains the driver's brake force command from the pedal sensor, the vehicle speed from onboard sensor or speed estimator, and the battery SOC and temperature from the BMS. The ideal braking force distribution law gives the front brake force and the rear brake force in real time, respectively. Then, the controller determines the desired regenerative brake force according to the fuzzy rules.

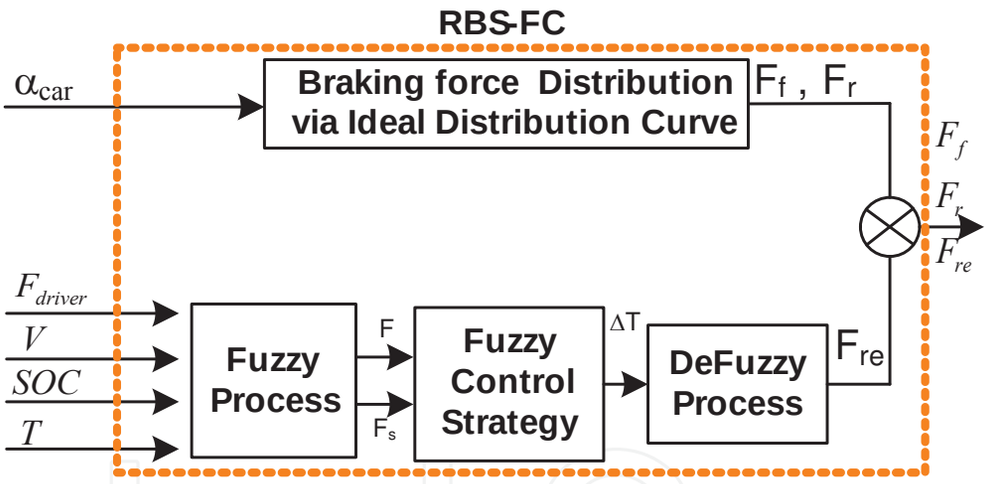

Figure 21. Structure of the control strategy system

5.2.3. Results

The proposed RBS-FC was verified in an EV prototype [22] (see Figure 22). In the test, we drove the EV on an urban road without and with RBS-FC function, respectively. The comparative results are shown in Figure 23 and Table 2, which verify that both the component efficiency and the maximum driving range are improved significantly with the proposed RBS-FC compared to the non-RBS-FC operation. The overall energy efficiency is improved from 0.341 to 0.417, i.e., an improvement of about 22%. The immediate benefit is that the maximum driving range of LF620 EV is extended from 163 kilometers to 205 kilometers for a single charge, i.e., a 26% improvement.

http://dx.doi.org/10.5772/59420

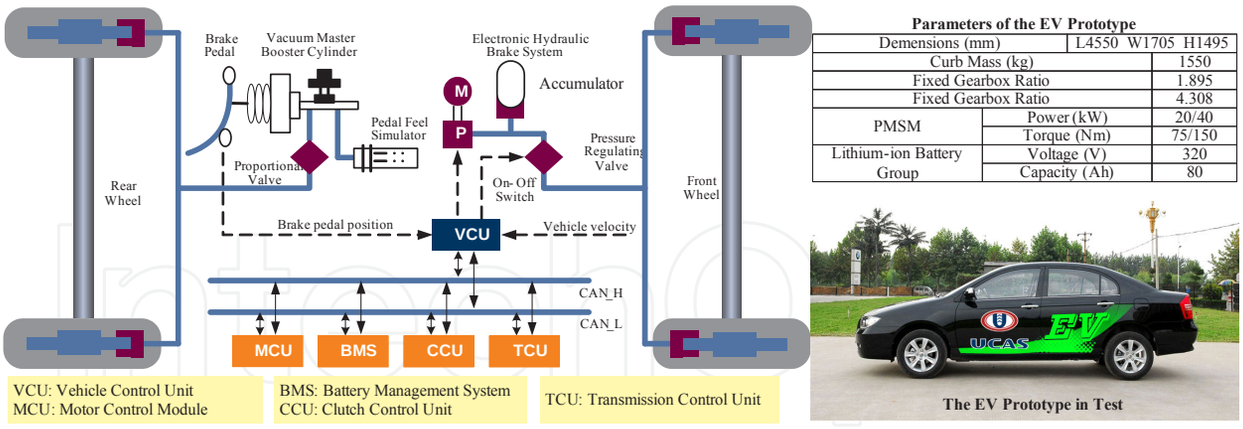

Figure 22. The test EV prototype

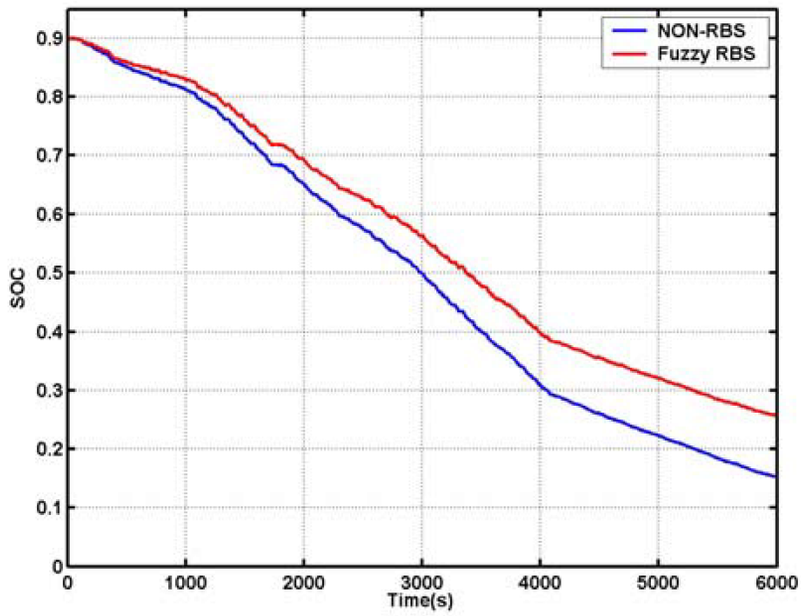

Figure 23. Comparative result of the SOC

	WITHOUT RBS-FC	WITH RBS-FC	Improvement
Motor/Controller Efficiency	0.67	0.78	16.4%
Overall Energy Efficiency	0.341	0.417	22.2%
Maximum Driving Range (km)	163	205	25.7%

Table 2. Comparison of the experimental results

6. EV energy management and optimization

6.1. Introduction of EV energy management

The energy management here is mainly targeted at the hybrid vehicles. Hybrid vehicles use two or more than two kinds of power sources, thus the energy management strategy of hybrid vehicles is one of the most important and popular research topics, as it determines the power split between power sources and because it is related to the fuel economy of the hybrid vehicles. Several types of energy management strategies for hybrid vehicles have been developed during last few decades. These strategies can be divided into two major groups: one is on the basis of the heuristic concept; the other is based on the optimal control theory. The former mainly includes rule-based algorithms and fuzzy logic algorithms [2, 34]. Earlier in the development of hybrid vehicles, energy management strategies were dominated by these types of strategies owing to their simplicity when actually realizing them. These types of strategies, however, cannot guarantee the optimal power distribution between power sources and the optimal fuel economy as well. In addition, the rules and fuzzy logics need expert knowledge. To remedy this problem, the optimal control theory was introduced as part of the energy management strategy of hybrid vehicles, including both Dynamic Programming (DP) as developed by R. E. Bellman [35] and Pontryagin's Minimum Principle (PMP) [36-38]. The DP approach examines all admissible control inputs at every state, thus guaranteeing global optimality if the driving cycle information is given in advance [35]. However, the DP approach cannot be used directly for the real-time control of hybrid vehicles due to the backward-looking calculation process and the long calculation time. Being confronted with the drawbacks of the DP, some researchers have proposed stochastic dynamic programming (SDP) [39, 40] to overcome these problems. The PMP-based energy management strategy optimizes the power distribution between power sources and minimizes the performance measure by instantaneously providing the necessary optimality conditions. One of the major advantages of the PMP-based strategy is that there is usually one parameter to be tuned in this strategy in order to obtain optimal results over a specific driving cycle [36]. Moreover, the core of this strategy is implementable in a real-time controller, even if the driving cycle information is not known in advance [37]. Furthermore, previous research [41] proved from a mathematical point of view that the PMP-based energy management strategy can serve as a global optimal solution (DP) under the assumption that the OCV and the internal resistance of a battery are independent of the battery SOC. This assumption is reasonable for charge-sustaining types of hybrid vehicles, especially for those which use lithium-ion batteries.

6.2. Energy management based on optimal control theory

In this sub-section, two types of optimal control theory-based energy management strategies of hybrid vehicles are introduced which are the DP approach and the PMP-based strategy, respectively. The simulation results regarding the two energy management strategies are also presented.

http://dx.doi.org/10.5772/59420

6.2.1. The vehicle model

An FCHV is selected as an example to introduce the two energy management strategies. Figure 24 [42] shows the block diagram of an FCHV in which an FCS and a battery are the two power sources. The electrical energy provided by the FCS and the battery is converted to the mechanical energy through the electric motor to propel the vehicle. Meanwhile, the electric motor can be controlled to work as a generator to convert a part of braking energy of the vehicle to electrical energy and store it into the battery. A group of vehicle parameters are selected by consulting the available literature [43] for the simulation study as listed in Table 3. The powertrain information is also summarized in Table 3. Details on this vehicle model can be found in the literature [42, 44, 45].

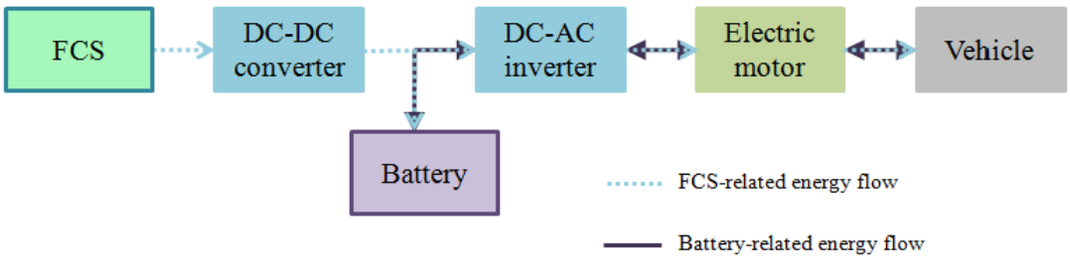

Figure 24. Configuration and energy flow of an FCHV

Parameter	Value
Vehicle total mass (kg)	1500
Final drive gear efficiency (%)	95
Tire radius (m)	0.29
Aerodynamic drag coefficient	0.37
Vehicle frontal area (m^2)	2.59
Air density (kg/m^3)	1.21
Rolling resistance coefficient	0.014
Electric motor (kW)	75
FCS (kW)	45
Battery (kWh)	1.9
Efficiency of converter and inverter (%)	95

Table 3. Vehicle parameters and powertrain information of the FCHV

6.2.2. DP approach

The DP examines all possible control inputs at every state [46]. Thus, the optimal trajectory to the final state can be obtained for every state in the DP. The DP needs much more calculation time compared to the PMP due to above characteristics.

The objective of the optimal control problem here is to find an optimal power split ratio trajectory during driving which brings the minimum fuel consumption. Here, we define the battery power P_{bat} as the control variable and the battery SOC as the state variable. The state equation of the optimal control problem expresses the dynamic behavior of the battery as shown in (19), in which Q_{bat} is the capacity and V is the open circuit voltage and R is the internal resistance of the battery.

$$\begin{aligned} \dot{SOC} &= -\frac{1}{Q_{bat}} \frac{V(SOC) - \sqrt{V(SOC)^2 - 4R(SOC) \cdot P_{bat}}}{2R(SOC)} \\ \dot{SOC} &= f(P_{bat}, SOC) \end{aligned} \tag{19}$$

Now, we rewrite (19) in a discrete form as (20):

$$x(k+1) = x(k) + \Delta t \cdot f(u, x) \qquad k = 0, 1, \cdots, N-1 \tag{20}$$

Here, x is the state variable and u is the control variable. N is the number of time steps and f is the same function as in (19).

The performance measure J to be minimized here is the total fuel consumption. Optimal performance measure from every possible state at every time step to the designated final state can be expressed as follows:

$$\begin{aligned} &J^*_{N-k,N}(x(N-k)) = \min_{u(N-k)} (\Delta t \cdot \dot{m}_{h_2}(x(N-k), u(N-k)) + J^*_{N-(k-1),N}(x(N-(k-1)))) \\ &x(N-(k-1)) = x(N-k) + \Delta t \cdot f(u(N-k), x(N-k)) \\ &k = 0, 1, \cdots, N-1 \end{aligned} \tag{21}$$

Here, $\dot{m}_{h_2}$ is the fuel consumption rate of the FCS. $J^*_{N-k,N}$ represents the optimal performance measure from $N-k$ time step to the final time step N for every possible state at $N-k$ time step. The DP examines all possible control variables at every state and selects the optimal one to every state. $J^*_{N-(k-1),N}$ represents the optimal performance measure from $N-(k-1)$ time step to the final time step N for every possible state at $N-(k-1)$ time step.

Due to the calculation characteristics of the DP, the optimal results can be acquired only when the DP calculation is finished. The results of the DP form a field which is defined as the optimal field here. The optimal field includes not only the optimal state trajectory information but also the optimal performance measure information. Figure 25 illustrates an example of the optimal field of the FTP72 urban driving cycle. Here, the initial battery SOC and final SOC are all set to 0.6, and the line on the optimal field indicates the optimal trajectory of the battery SOC.

http://dx.doi.org/10.5772/59420

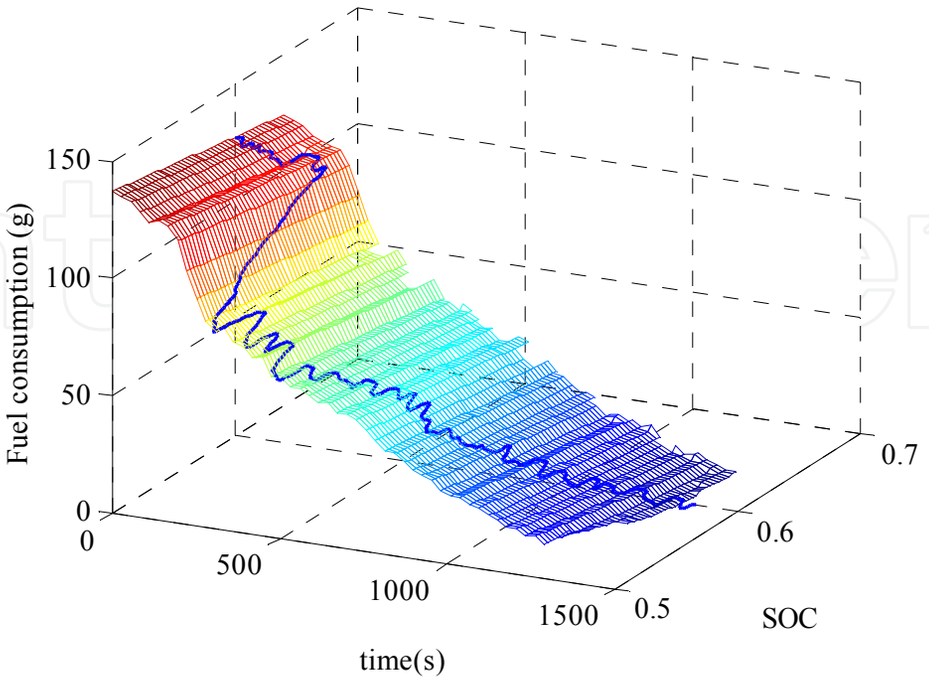

Figure 25. The optimal field of the FTP72 urban driving cycle

6.2.3. PMP-based strategy

The PMP-based energy management strategy optimizes the power distribution between the FCS and the battery instantaneously by providing the necessary optimality conditions. Here, we define the FCS net power P_{fcs} as the control variable, whereas the control variable in 5.2.2 is the battery power P_{bat}. The state equation of the control system is given in equation (19). Here, the time derivative of the battery SOC is expressed by P_{fcs} and the battery SOC instead of P_{bat} and SOC, as the total power requirement of the vehicle can be obtained when a driving cycle is given in advance. Therefore, the state equation of the optimal control problem is transformed using another function F, as follows:

$$\dot{SOC} = F(P_{fcs}, SOC) \tag{22}$$

Considering the state equation (22), which is also a constraint on the optimal control problem, and the relationship between P_{fcs} and $\dot{m}_{h_2}$, the performance measure is as follows:

$$J = \int_{t_0}^{t_f} \left\{ \dot{m}_{h_2}(P_{fcs}) + p \cdot \left(F - \dot{SOC} \right) \right\} dt \tag{23}$$

Here, p is the Lagrange multiplier, which is also defined as the co-state in the PMP and is an equivalent parameter between the fuel usage and the electric usage.

According to the optimal control theory based on the Calculus of Variation, the necessary conditions of the optimal control problem can be obtained when the variation of the performance measure δJ is zero [46]. If we introduce a Hamiltonian H, which is defined as

$$H = \dot{m}_{h_2}(P_{fcs}) + p \cdot F(P_{fcs}, SOC), \tag{24}$$

then the necessary conditions that minimize the performance measure (23) from time t_0 to time t_f are as follows:

$$\begin{aligned} \frac{\partial H}{\partial p} &= \dot{SOC} \\ \frac{\partial H}{\partial SOC} &= -\dot{p} \\ \frac{\partial H}{\partial P_{fcs}} &= 0 \end{aligned} \tag{25}$$

The first necessary condition in (25) is the state equation. The second necessary condition is the co-state equation, which determines the optimal trajectory of the co-state p. The third necessary condition determines the optimal trajectory of the control variable P_{fcs} by minimizing the Hamiltonian H.

The PMP is the general case of the Calculus of Variation, in which the third necessary condition in (25) is expressed as follows:

$$H(P_{fcs}^*, SOC^*, p^*) \le H(P_{fcs}, SOC^*, p^*) \tag{26}$$

The advantage of this form is that it can be applied to non-linear or non-differentiable or non-convex function [41].

Figure 26 [47] illustrates an example of solving the optimal solution according to the PMP. From the shape of the third subplot, it can be observed that the optimal FCS net power can be obtained at this moment, which minimizes the Hamiltonian. The similar process is repeated at every calculation time step, and the optimal solution trajectory can be obtained finally.

6.2.4. Comparison of PMP-based strategy and DP approach

Simulation results of the above two energy management strategies are compared on three typical driving cycles here. The first subplot in Figure 27 [48] illustrates the optimal battery SOC trajectories on the FTP72 urban driving cycle solved by the PMP and the DP. As we can

http://dx.doi.org/10.5772/59420

see, the two trajectories overlap each other most of the time. However, the two trajectories are not perfectly the same. Different calculation environment for each energy management strategy may have influence on this fact. The trajectories will be closer to each other if the same calculation environment is used. The second and the third subplots in Figure 27 are for the cases of the NEDC 2000 and the Japan 1015 driving cycle, respectively. Table 4 [48] shows the fuel economy comparison of the two energy management strategies. As we can see, the discrepancy between the two strategies is within 0.5 % for the three driving cycles.

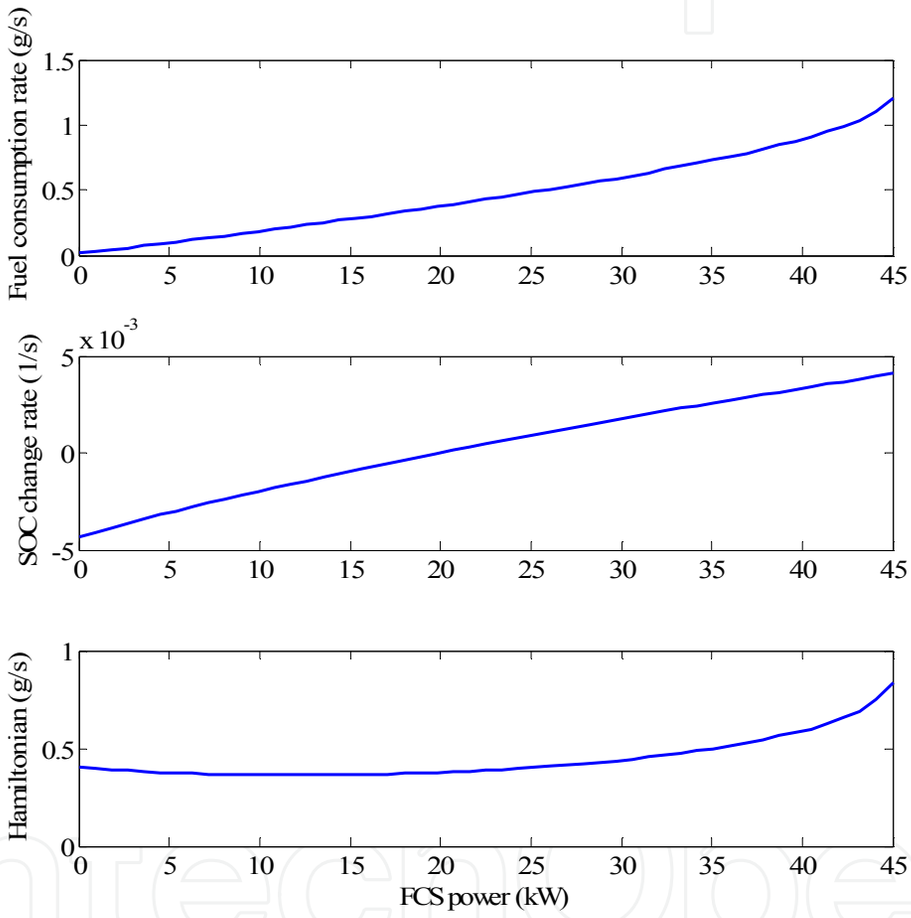

Figure 26. An example of solving the optimal FCS net power according to the PMP

	FTP72 urban	NEDC 2000	Japan 1015
DP (kg/100 km)	1.063	1.195	1.012
PMP (kg/100 km)	1.064	1.195	1.017
Discrepancy (%)	0.094	0	0.494

Table 4. Fuel economy comparison between DP and PMP

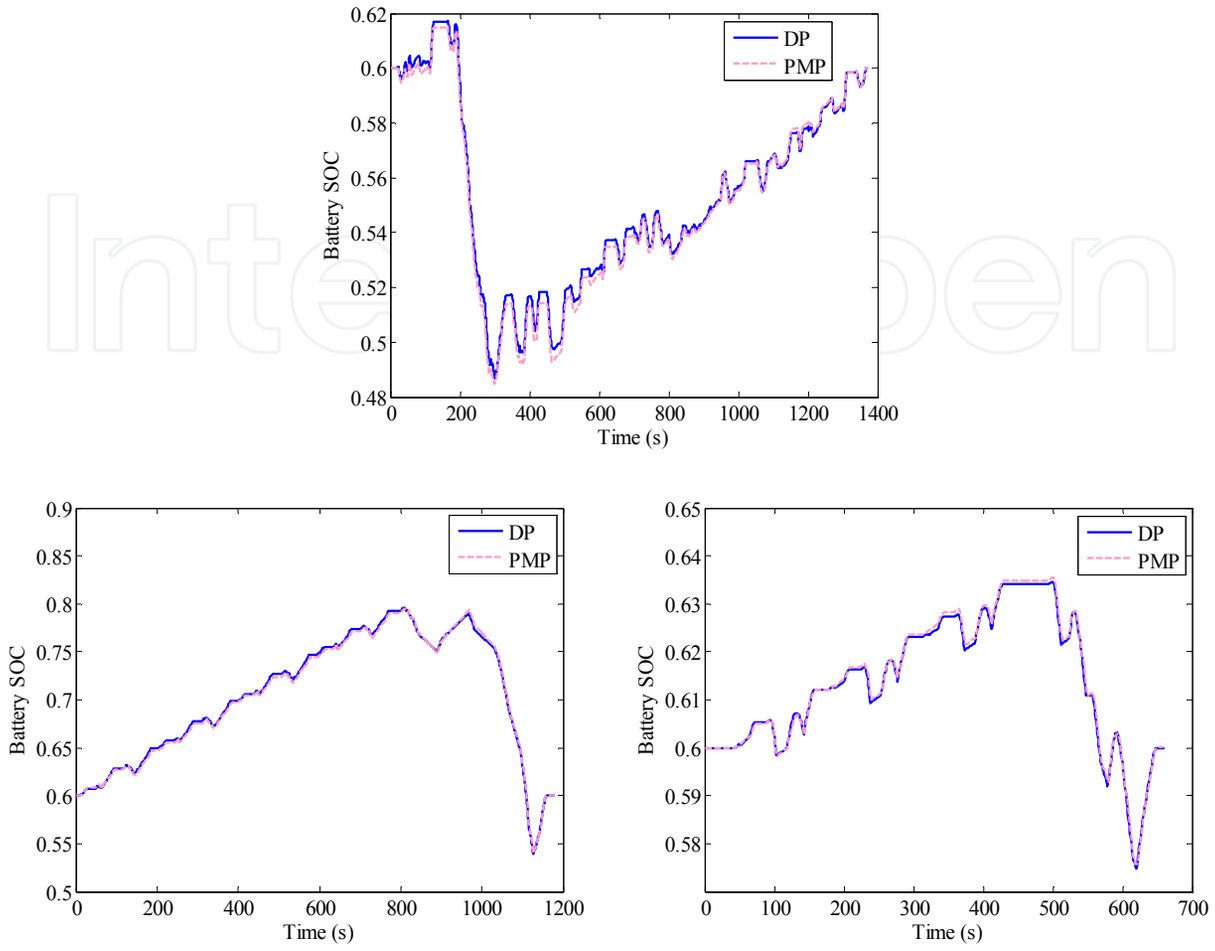

Figure 27. Comparison of DP and PMP on the optimal battery SOC trajectories

6.3. Energy management using prediction of future driving condition

In 5.2, the energy management strategies are evaluated on some specific driving cycles. However, the driving cycle is not fixed in the real-world driving. Currently, the vehicle telemetry, such as the Global Positioning System (GPS) and the Intelligent Transportation System (ITS), is actively used to vehicles in order to provide traffic preview information to the drivers. This information can be used when constructing energy management strategies of hybrid vehicles. In this section, the PMP-based energy management strategy introduced in 5.2.3 is extended in order to optimize the power distribution and as well as the vehicle driving route based on the traffic preview information.

The control objective here is to optimize the vehicle driving route and the power split ratio at the same time using the traffic preview information, so that the fuel consumption is further minimized. There are two state variables in this control problem, which are the battery SOC and the vehicle velocity v_{veh}. The two state equations are as follows:

http://dx.doi.org/10.5772/59420

$$\begin{aligned} \dot{SOC} &= f\left(SOC, P_{fcs}, v_{veh}, a_{veh}\right) \\ \dot{v}_{veh} &= a_{veh} \end{aligned} \tag{27}$$

The first equation in (27) is the dynamic behavior of the battery, and the second equation represents the vehicle dynamic behavior. Here, the FCS net power P_{fcs} and the vehicle acceleration a_{veh} are two control variables of the control problem.

Constraints on the state variables and on the control variables are as follows:

$$\begin{aligned} &SOC_{\min} \le SOC(t) \le SOC_{\max} \\ &v_{\min}(t) \le v_{veh}(t) \le v_{\max}(t) \\ &P_{fcs,\min}(t) \le P_{fcs}(t) \le P_{fcs,\max}(t) \\ &a_{\min}(t) \le a_{veh}(t) \le a_{\max}(t) \\ &\int_{t_0}^{t_f} v_{veh}(t)dt = L \end{aligned} \tag{28}$$

Here, t_0 and t_f are the initial time and final time of the preview length, and L is the preview length. L, $v_{\min}$, and $v_{\max}$ can be obtained from the GPS and ITS devices. The battery SOC constraint is time-invariant, and the maximum and minimum values of other cases are time-variant.

The application process of the PMP for the two-state variable system is similar to that for a single state variable system. According to the PMP, when a Hamiltonian is defined as follows

$$H\left(SOC, P_{fcs}, v_{veh}, a_{veh}\right) = \dot{m}_{h_2}\left(P_{fcs}\right) + p_1 \cdot f\left(SOC, P_{fcs}, v_{veh}, a_{veh}\right) + p_2 \cdot a_{veh}, \tag{29}$$

the necessary conditions that can achieve the goal of this control problem are as follows:

$$\begin{aligned} \dot{SOC}^* &= \frac{\partial H}{\partial p_1}\left(SOC^*, P_{fcs}{}^*, v_{veh}{}^*, a_{veh}{}^*\right) \\ \dot{v}_{veh}{}^* &= \frac{\partial H}{\partial p_2}\left(SOC^*, P_{fcs}{}^*, v_{veh}{}^*, a_{veh}{}^*\right) \\ \dot{p}_1^* &= -\frac{\partial H}{\partial SOC}\left(SOC^*, P_{fcs}{}^*, v_{veh}{}^*, a_{veh}{}^*\right) \\ \dot{p}_2^* &= -\frac{\partial H}{\partial v_{veh}}\left(SOC^*, P_{fcs}{}^*, v_{veh}{}^*, a_{veh}{}^*\right) \\ H\left(SOC^*, P_{fcs}{}^*, v_{veh}{}^*, a_{veh}{}^*, p_1^*, p_2^*\right) &\le H\left(SOC^*, P_{fcs}, v_{veh}{}^*, a_{veh}, p_1^*, p_2^*\right) \end{aligned} \tag{30}$$

Here, the first two necessary conditions are the two state equations, which are also constraints on the optimal control problem. p_1 and p_2 are two co-states which can be determined based on the third and the fourth necessary conditions. At every calculation time step, the optimal FCS net power and the optimal vehicle acceleration can be found by the fifth necessary condition.

Figure 28 [49] illustrates an example of simulation results. A FCHV with the total mass of 1700kg is used in this simulation. This figure shows the maximum and the minimum vehicle velocities along the preview driving which are assumed to be provided by the GPS and ITS devices. This figure also shows a benchmark vehicle velocity profile, which is within the above two velocity profiles, and the optimal vehicle velocity profile derived from the proposed energy management strategy. The length discrepancy between the optimal and the benchmark vehicle velocity profiles is around three meters here. The fuel economy is improved through the proposed energy management strategy compared to the benchmark case. In the benchmark case, the vehicle velocity profile is fixed and only the power split ratio is optimized. Table 5 [49] shows the fuel consumption information of the two vehicle velocity profiles. This table reflects that the fuel consumption is improved around 10.4 % by the proposed energy management strategy.

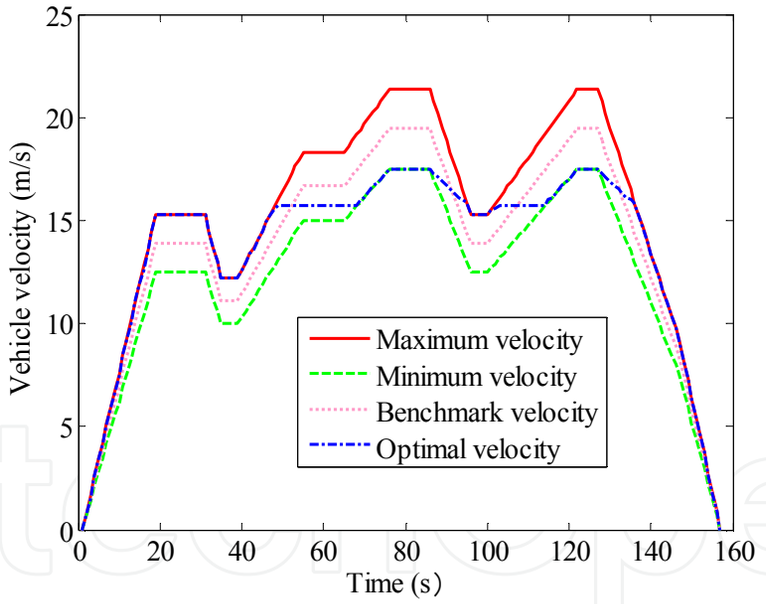

Figure 28. The optimal vehicle velocity profile and the benchmark velocity profile

	Fuel consumption (kg/100km)	Driving distance (m)
Benchmark velocity profile	1.030	2173
Optimal velocity profile	0.923	2170

Table 5. Fuel consumption of the optimal vehicle velocity profile and the benchmark velocity profile

http://dx.doi.org/10.5772/59420

7. Conclusions

This chapter deals with the energy processing and control of EVs. The latest energy saving and optimal control technologies are introduced and the key results contributed by the authors on the high-efficiency traction motor, intelligent battery management system, regenerative braking with high energy recovery, and the vehicle energy management are presented. The following points are drawn from this chapter:

1. For the integrated motor drive study, the integrated SRM drive obtains the battery charger and grid-connected inverter functions, whereas it saves the cost, space, and weight. The TDM method is used to improve the coefficient of utilization of the components. The suitable parking position is discussed for the stable working in the bi-directional mode. The power factor correction is considered and well worked in the integrated SRM drive.

2. For the BMS study, the proposed quantitative relationship exhibits the functions of the terminal voltage, resting time, and temperature to the initial battery SOC. This achievement raises the accuracy of the battery SOC estimation system and improves match flexibility between the battery SOC and the power output. The correlation analysis result of the energy efficiency shows that there is a parabola relationship between the energy efficiency and the DOD under the constant current rate. The battery energy conversion efficiency is less influenced by the thermal effect under the smaller current rate.

3. For the RBS study, the comparative results verify that both the component efficiency and the maximum driving range are improved significantly with the proposed RBS-FC compared to the non-RBS-FC operation. The overall energy efficiency is improved around 22%. The immediate benefit is that the maximum driving range of LF620 EV is extended from 163 kilometers to 205 kilometers for a single charge, i.e., a 26% improvement.

4. For the energy management and optimization study, the PMP-based strategy obtains almost the same optimal trajectories with the DP approach, while it saves much more computation time compared to the DP approach. The extended PMP-based strategy, which optimizes the power distribution and as well as the vehicle driving route based on the traffic preview information, improves the fuel economy around 10.4 % compared to a benchmark case studied in this chapter.

Acknowledgements

This work was supported by National Natural Science Foundation of China (Grant No. 51305437 and No. 51107142), Shenzhen Basic Research Fund (JCYJ20130401170306801, JCYJ20120617121836364, JCYJ20130401170306854), and Guangdong Innovative Research Team Program (No. 201001D0104648280).

Author details

Guoqing Xu[1,2], Chunhua Zheng[1,2*], Yanhui Zhang[1], Kun Xu[3] and Jianing Liang[1]

*Address all correspondence to: ch.zheng@siat.ac.cn

1 Automotive Electronics Research Center, Shenzhen Institutes of Advanced Technology, Chinese Academy of Sciences, Shenzhen, China

2 Department of Mechanical and Automation Engineering, The Chinese University of Hong Kong, Hong Kong, China

3 Shenzhen College of Advanced Technology, University of Chinese Academy of Sciences, Shenzhen, China

References

[1] Chan CC, Bouscayrol A, Chen K. Electric, Hybrid, and Fuel-cell Vehicles: Architectures and Modeling. IEEE Transactions on Vehicular technology 2010; 59(2) 589-598.

[2] Ehsani M, Gao Y, Emadi A. Modern Electric, Hybrid Electric, and Fuel Cell Vehicles. Boca Raton: CRC Press; 2010.

[3] Chan CC. The State of the Art of Electric, Hybrid, and Fuel Cell Vehicles. Proceeding of the IEEE 2007; 95(4) 704-718.

[4] Dyke KJ, Schofield N, Barnes M. The impact of transport electrification on electrical networks. IEEE Trans. Ind. Electron. 2010; 57(12) 3917-3926.

[5] Mapelli FL, Tarsitano D, Mauri M. Plug-in hybrid electric vehicle: modeling, prototype, realization, and inverter losses reduction analysis. IEEE Trans. Ind. Electron. 2010; 57(2) 598-607.

[6] Saber AY, Venayagamoorthy GK. Plug-in vehicles and renewable energy sources for cost and emission reductions. IEEE Trans. Ind. Electron. 2011; 58(4) 1229-1238.

[7] Wieringen V, Pop-Iliev R. Development of a dual-fuel power generation system for an extended range plug-in hybrid electric vehicle. IEEE Trans. Ind. Electron. 2010; 57(2) 641-648.

[8] Sul SK, Lee SJ. An integral battery charger for four wheel drive electric vehicle. IEEE Trans. Ind. Appl. 1995; 31(5) 1096-1099.

[9] Pellegrino G, Armando E, Guglielmi P. An integral battery charger with power factor correction for electric scooter. IEEE Trans. Pow. Electron. 2010; 25(3) 751-759.

[10] Liang J, Lee DH, Xu G, Ahn JW. Analysis of passive boost power converter for three-phase SR drive. IEEE Transactions on Industrial Electronics 2010; 57(9) 2961-2971.

[11] Chang HC, Liaw CM. Development of a compact switched-reluctance motor drive for EV propulsion with voltage-boosting and PFC charging capabilities. IEEE Transactions on Vehicular Technology 2009; 58(7) 3198-3215.

[12] Liang J, Xu G, Wang B, Wang H. A Novel Integrated Switched Reluctance Motor Drive with Bi-directional Inverter: proceedings of IEEE International Conference on Industrial Technology, 26 Feb.-1 Mar. 2014, Busan, Korea.

[13] Liang J, Xu G, Jian L, Chang M. Analysis Parking Position of Integrated Switched Reluctance Motor Drive System with On-board Charger for EV: proceedings of the 8th IEEE Vehicle Power and Propulsion Conference, 9-12, Oct. 2012, Seoul, Korea.

[14] Li JH, Barillas JK, Guenther C, Danzer MA. A Comparative Study of State of Charge Estimation Algorithms for LiFePO4 Batteries Used in Electric Vehicles. Journal of Power Sources 2013; 230 244-250.

[15] Zhang YH, Song WJ, Lin SL, Lv J, Feng ZP. A Critical Review on State of Charge of Batteries. Journal of Renewable and Sustainable Energy 2013; 5(2) 021403-1-021403-10.

[16] He HW, Zhang XW, Xiong R, Xu Y, Guo Hq. Online Model-Based Estimation of State of Charge and Open Circuit Voltage of Lithium Ion Batteries in Electric Vehicles. Energy 2012; 39(1) 310-318.

[17] He HW, Xiong R, Guo HQ. Online Estimation of Model Parameters and State-of-Charge of LiFePO4 Batteries in Electric Vehicles. Applied Energy 2012; 89(1) 413-420.

[18] Thomas KE, Bogatu C, Newman J. Measurement of the Entropy of Reaction as a Function of State of Charge in Doped and Undoped Lithium Manganese Oxide. Journal of the Electrochemical Society 2001; 148(6) A570-A575.

[19] Onda K, Kameyama H, Hanamoto T, Ito K. Experimental Study on Heat Generation Behavior of Small Lithium-Ion Secondary Batteries. Journal of the Electrochemical Society 2003; 150(3) A285-A291.

[20] Bandhauer TM, Garimella S, Fuller TF. A Critical Review of Thermal Issues in Lithium-Ion Batteries. Journal of the Electrochemical Society 2011; 158(3) R1-R25.

[21] Gao YM, Chen LP, Ehsani M. Investigation of the effectiveness of regenerative braking for EV and HEV. SAE Trans 1999; 108 3184-3190.

[22] Xu GQ, Li WM, et al. An Intelligent Regenerative Braking Strategy for Electric Vehicles. Energies 2011; 4(9) 1461-1477.

[23] Yao J, Zhong ZM, Sun ZC. A fuzzy logic based regenerative braking regulation for a fuel cell bus: proceedings of the IEEE International Conference on Vehicular Electronics and Safety, 13-15 December 2006, Beijing, China.

[24] Zolot M, Markel T, Pesaran A. Analysis of fuel cell vehicle hybridization and implications for energy storage devices: proceedings of the 4th Advanced Automotive Battery Conference, 2-4 June 2004, San Francisco, CA, USA.

[25] Yin GD, Jin XJ. Cooperative Control of Regenerative Braking and Antilock Braking for a Hybrid Electric Vehicle. Mathematical Problems in Engineering 2013; 1-9.

[26] Guo HQ, He HW, et al. A Combined Cooperative Braking Model with a Predictive Control Strategy in an Electric Vehicle. Energies 2013; 6(12) 6455-6475.

[27] Zhang CW, Bai ZF, Cao BG, Li JC. Study on regenerative braking of electric vehicle: proceedings of the 4th International Power Electronics and Motion Control Conference, 14-16 August 2004, Xi'an, China.

[28] Guo JG, Wang JP, Cao BG. Regenerative braking strategy for electric vehicles: proceeding of the 2009 IEEE Intelligent Vehicles Symposium, 3-5 June 2005, Xi'an, China.

[29] Zhang JM, Song BY, Cui SM. Fuzzy logic approach to regenerative braking system: proceedings of the International Conference on Intelligent Human-Machine Systems and Cybernetics, 26-27 August 2009, Hangzhou, China.

[30] Paterson J, Ramsay M. Electric vehicle braking by fuzzy logic control: proceedings of the IEEE Industry Applications Society Annual Meeting, 2-8 October 1993, Toronto, Canada.

[31] Ye M, Bai Z, Cao B. Robust Control for Regenerative Braking of Battery Electric Vehicle. IET Control Theory and Applications 2008; 2(12) 1105-1114.

[32] Gao HW, Gao YM, Ehsani M. A neural network based SRM drive control strategy for regenerative braking in EV and HEV: proceedings of the Electric Machines and Drives Conference, 17-20 June 2001, Cambridge, MA, USA.

[33] Mutoh, N, Hayano Y, Yahagi H, Takita K. Electric braking control methods for electric vehicles with independently driven front and rear wheels. IEEE Transactions on Industrial Electronics. 2007; 54(2) 1168-1176.

[34] Gao DW, Jin ZH, Lu QC. Energy Management Strategy Based on Fuzzy Logic for a Fuel Cell Hybrid Bus. Journal of Power Sources 2008; 185(1) 311-317.

[35] Lin CC, Peng H, Grizzle JW, Kang J. Power Management Strategy for a Parallel Hybrid Electric Truck. IEEE Transactions on Control Systems Technology 2003; 11(6) 839-849.

[36] Serrao L, Rizzoni G. Optimal control of power split for a hybrid electric refuse vehicle: proceedings of American Control Conference, 11-13 June 2008, Washington, USA.

[37] Chasse A, Sciarretta A. Supervisory Control of Hybrid Powertrains: an Experimental Benchmark of Offline Optimization and Online Energy Management. Control Engineering Practice 2011; 19(11) 1253-1265.

[38] Kim NW, Cha SW, Peng H. Optimal Equivalent Fuel Consumption for Hybrid Electric Vehicles. IEEE Transactions on Control Systems Technology 2012; 20(3) 817-825.

[39] Lin CC, Peng H, Grizzle JW. A stochastic control strategy for hybrid electric vehicles: proceedings of American Control Conference, 30 June-2 July 2004, Boston, USA.

[40] Kim MJ, Peng H. Power Management and Design Optimization of Fuel Cell/Battery Hybrid Vehicles. Journal of Power Sources 2007; 165(2) 819-832.

[41] Kim NW, Cha SW, Peng H. Optimal Control of Hybrid Electric Vehicles Based on Pontryagin's Minimum Principle. IEEE Transactions on Control Systems Technology 2011; 19(5) 1279-1287.

[42] Zheng CH, Xu GQ, Cha SW, Park YI, Lim WS. PMP-Based Power Management Strategy for Two-State Variable FCHV Systems and Its Optimality. International Journal of Precision Engineering and Manufacturing 2014; 15(4) 769-776.

[43] Bernard J, Delprat S, Buechi F, Guerra TM. Fuel-Cell Hybrid Powertrain: Toward Minimization of Hydrogen Consumption. IEEE Transactions on Vehicular Technology 2009; 58(7) 3168-3176.

[44] Zheng CH, Kim NW, Cha SW. Optimal Control in the Power Management of Fuel Cell Hybrid Vehicles. International Journal of Hydrogen Energy 2012: 37(1) 655-663.

[45] Zheng CH, Xu GQ, Park YI, Lim WS, Cha SW. Prolonging Fuel Cell Stack Lifetime Based on Pontryagin's Minimum Principle in Fuel Cell Hybrid Vehicles and Its Economic Influence Evaluation. Journal of Power Sources 2014; 15 533-544.

[46] Kirk DE. Optimal Control Theory. New York: Prentice-Hall; 1970.

[47] Zheng CH, Oh CE, Park YI, Cha SW. Fuel Economy Evaluation of Fuel Cell Hybrid Vehicles Based on Equivalent Fuel Consumption. International Journal of Hydrogen Energy 2012: 37(2) 1790-1796.

[48] Zheng CH, Park YI, Lim WS, Cha SW, Xu GQ. Comparison of PMP and DP in Fuel Cell Hybrid Vehicles. International Journal of Automotive Technology 2014: 15(1) 117-123.

[49] Zheng CH, Xu GQ, Cha SW. A power management strategy of hybrid vehicles using traffic preview information: proceedings of Vehicular Technology Conference 2014-Spring, 18-21 May 2014, Seoul, Korea.

IntechOpen